

# Accounting for reporting delays in real-time phylodynamic analyses with preferential sampling

Catalina M. Medina<sup>1</sup>, Julia A. Palacios<sup>2</sup>, Volodymyr M. Minin<sup>1\*</sup>

<sup>1</sup>Department of Statistics, University of California, Irvine,

<sup>2</sup>Departments of Statistics and Biomedical Data Science, Stanford University,

\*vminin@uci.edu

## Abstract

The COVID-19 pandemic demonstrated that fast and accurate analysis of continually collected infectious disease surveillance data is crucial for situational awareness and policy making. Coalescent-based phylodynamic analysis can use genetic sequences of a pathogen to estimate changes in its effective population size, a measure of genetic diversity. These changes in effective population size can be connected to the changes in the number of infections in the population of interest under certain conditions. Phylodynamics is an important set of tools because its methods are often resilient to the ascertainment biases present in traditional surveillance data (e.g., preferentially testing symptomatic individuals). Unfortunately, it takes weeks or months to sequence and deposit the sampled pathogen genetic sequences into a database, making them available for such analyses. These reporting delays severely decrease precision of phylodynamic methods closer to present time, and for some models can lead to extreme biases. Here we present a method that affords reliable estimation of the effective population size trajectory closer to the time of data collection, allowing for policy decisions to be based on more recent data. Our work uses readily available historic times between sampling and sequencing for a population of interest, and incorporates this information into the sampling model to mitigate the effects of reporting delay in real-time analyses. We illustrate our methodology on simulated data and on SARS-CoV-2 sequences collected in the state of Washington in 2021.

## 1 Introduction

The COVID-19 pandemic demonstrated that fast and accurate analysis of continually collected infectious disease surveillance data is crucial for situational awareness and policy making (Cori and Kucharski, 2024; Engebretsen et al., 2023). Phylodynamic methods form an important set of tools that use genetic sequences of a pathogen of interest to infer its phylogeny and parameters of disease dynamics, such as the effective population size. The effective population size is a measure of genetic diversity, and estimation of effective population size is often of interest because under certain conditions this quantity can be connected to the number of infections in the population (Volz et al., 2009) or in some cases more directly to transmission (Frost and Volz, 2010). Inference of the effective population size can also be useful to compare the growth of different viral lineages (Fountain-Jones et al., 2020; Volz et al., 2021), as one part of an argument for the effectiveness of an intervention (van Ballegooijen et al., 2009), and ultimately, for informed health policy decisions (Rich et al., 2023).

The COVID-19 pandemic resulted in a massive push towards sharing sampled pathogenic sequences in public databases such as: GISAID ([www.gisaid.org](http://www.gisaid.org)), NCBI ([www.ncbi.nlm.nih.gov](http://www.ncbi.nlm.nih.gov)), and ViPR ([www.viprbrc.org](http://www.viprbrc.org)). Unfortunately, collected samples can take weeks or even months to sequence and upload to a database, making them available for analysis (Kalia et al., 2021). We refer to this time between sample collection and sequence reporting as the *reporting delay* for a sample. Reporting delays result in missing data near present time since recently collected samples

are less likely to have been sequenced and uploaded yet. During the COVID-19 pandemic, reporting delays were a novel and important consideration to most, with the emerging need for real-time analysis, i.e., analysis conducted up to present time (Kalia et al., 2021). The distribution of delays can be location, time, and even lineage specific (Petroni et al., 2023), influenced by factors such as sequencing cost and laboratory limited capacity. Researchers who had considered reporting delays for surveillance data in real-time analyses, were limited to methods that utilized only aggregated level reporting delay information (Bastos et al., 2019). The shared public databases of pathogenic sequences provide a new opportunity to utilize detailed sequence-level data of reporting delays.

Modern methods to estimate effective population size changes from genetic data have evolved from the original coalescent skyline plot where the effective population size trajectory,  $N_e(t)$ , was modeled nonparametrically as piecewise constant (Pybus et al., 2000), to grouping methods that resulted in smoother estimates (Strimmer and Pybus, 2001), to the first Bayesian coalescent skyline plot model (Drummond et al., 2005) which jointly inferred a pathogen’s evolutionary tree and  $N_e(t)$ . Several advancements on the Bayesian coalescent skyline plot models have been proposed in recent years which consider different interval specifications for the piecewise  $N_e(t)$  or regularization methods for  $N_e(t)$ . See Billenstein and Höhna (2024) for a detailed comparison of Bayesian non-parametric inference of  $N_e(t)$  methods (Billenstein and Höhna, 2024). When pathogen samples are being continually collected over time it is often the case that the frequency at which samples are collected is related to the burden of the infection in the population. This is known as preferential sampling, and Karcher et al. (2016) proposed a phylodynamic model that built on Bayesian coalescent skyline plot models to relate the sampling intensity to the effective population size (Karcher et al., 2016). It was shown that unaccounted for preferential sampling can result in biases and accounting for preferential sampling can result in more accurate and precise inference of the effective population size trajectory. This model has been extended to allow for additional factors to be related to the sampling intensity and effective population size (Karcher et al., 2020; Cappello and Palacios, 2022).

In this work we use simulations to investigate the effects of reporting delays in real-time phylodynamic inference of the effective population size; we compare the effects across various state-of-the-art inferential strategies. We also propose a strategy to mitigate the effects of reporting delays within the preferential model, by incorporating information about the distribution of recent reporting delays. This extends the Karcher et al. (2020) model by including reporting probabilities into the sampling intensity model (Karcher et al., 2020). We use simulations to compare the performance of our proposed model with competitive real-time phylodynamic strategies in the presence of preferential sampling and reporting delays and show that our model has lower bias, better coverage, and higher precision than state-of-the-art methods. Finally, we use SARS-CoV-2 sequences from Washington state as a case study to compare real-time inferential strategies on data which suffers from reporting delays to the performance of retrospective inference on all sampled sequences in the hypothetical case of no reporting delays.

## 2 Methods

We will begin with a description of the nonparametric phylodynamic methodology proposed in Karcher et al. (2020) (Karcher et al., 2020). This Bayesian strategy will be described starting with how the pathogen genetic samples are modeled conditionally on its evolutionary tree, sampling times, number of samples at each time, and effective population size trajectory, followed by details of the overall full hierarchical model. Once this framework is understood, we will introduce our proposal to mitigate the effects of delays between collecting a sample and depositing a pathogen sequence obtained from the sample into a public database.

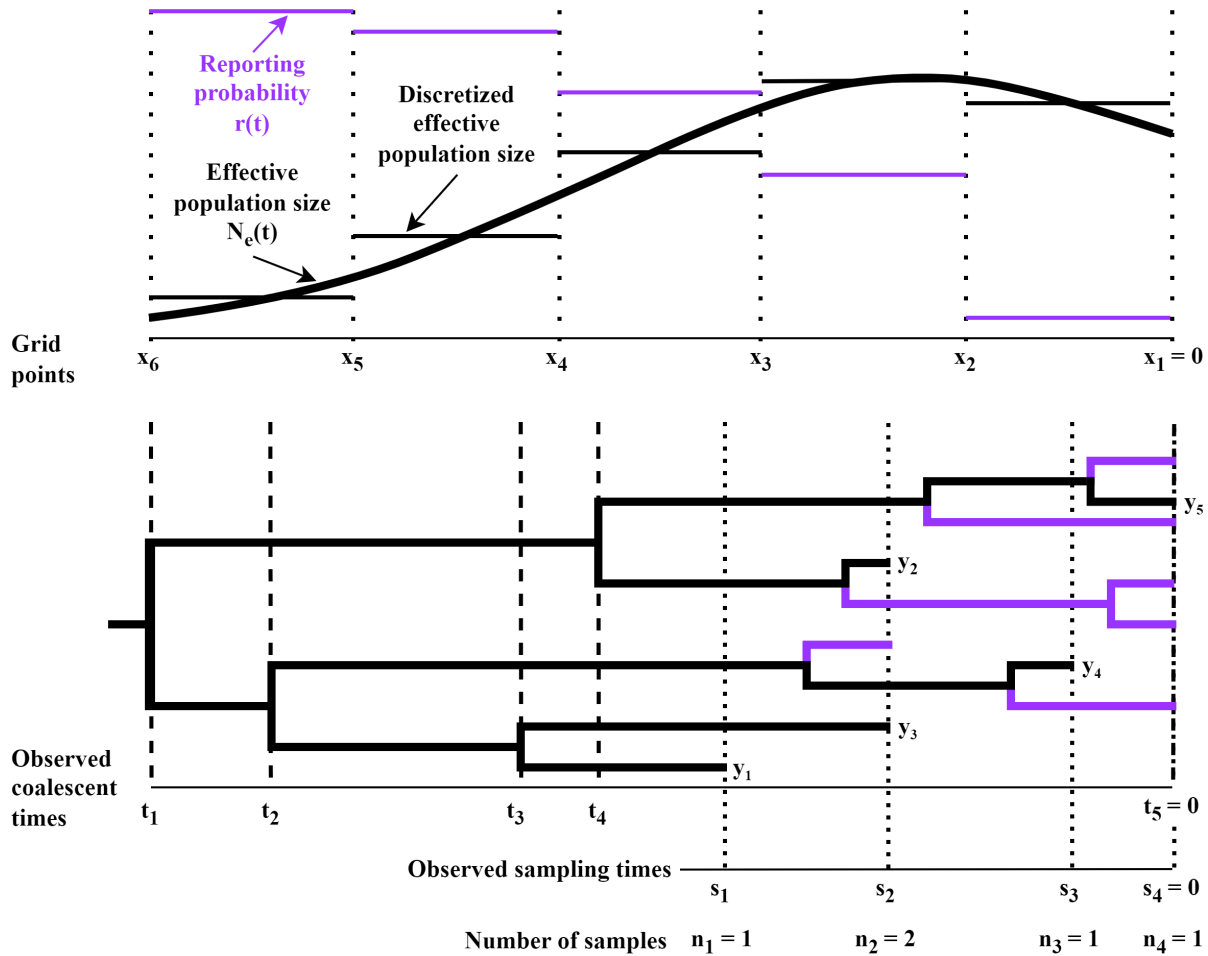


Figure 1: Example of an effective population size trajectory (top figure) and corresponding genealogy (bottom figure), with reporting probabilities and corresponding unobserved tips denoted by purple coloring. For a real-time analysis the reporting probability decreases as the collection date gets closer to present time, time zero.

## 2.1 Summary of Bayesian nonparametric $N_e(t)$ inference

When analyzing pathogen evolution, we use an alignment of sampled pathogen genetic sequences as data. These sequences can either be collected at the same time, isochronous sampling, or at different points in time, heterochronous sampling. Here we are concerned with viruses that evolve rapidly with continuously collected samples so we will consider heterochronous sampling of DNA or RNA sequences aligned and stored in matrix  $\mathbf{y} = \{y_{ji}\}$ ,  $j = 1, \dots, n$ ,  $i = 1, \dots, L$ , where  $n$  is the number of sequences and  $L$  is the alignment length. The sequences,  $\mathbf{y}$ , all ultimately share a common ancestry, and the evolution of the sequences from their most recent common ancestor is described by a bifurcating tree called a genealogy, denoted as  $\mathbf{g}$ .

We assume that given the genealogy, alignment sites are independent and identically distributed. The evolutionary changes in the nucleotides present at each alignment site, column of matrix  $\mathbf{y}$ , are modeled by a continuous-time Markov chain substitution model parameterized by vector  $\boldsymbol{\theta}$ . From a given viral genealogy and substitution rate matrix, the probability of observing sequences  $\mathbf{y}$ ,  $P(\mathbf{y}|\mathbf{g}, \boldsymbol{\theta})$  can be calculated using an efficient dynamic programming algorithm (Felsenstein, 1981). Equipped with a model for the alignment, a model is needed for the pathogen's genealogy.

The lower half of Fig 1 displays a genealogy relating five sequences, black tree tips, collected across four sampling times. Note the purple tips denote samples collected but not yet reported and available for use by the time of analysis. Sampling times are denoted by  $\mathbf{s} = \{s_j\}_{j=1}^m$  and sample sizes by  $\mathbf{n} = \{n_j\}_{j=1}^m$  with  $n = \sum_{j=1}^m n_j$ . In this set up we imagine generating the genealogy backwards in time starting from the most recent sampling time,  $s_m = 0$ . The branches of this evolutionary tree end at the sampling times  $\mathbf{s}$ , and the convergence, or coalescence, of two branches corresponds to a common ancestor of the two sequences. The tree's branches coalesce until the most recent common ancestor of all of the samples, the root of the tree. The times of the coalescent events are denoted  $\{t_i\}_{i=1}^{n-1}$ , with  $t_1 > \dots > t_{n-1}$ , and the last sampling time determines the last coalescent time,  $t_n = s_m = 0$ .

The effective population size, denoted  $N_e(t)$ , is a time-varying measure of genetic diversity. The number of active lineages at a time  $t$  is the difference between the number of sampling and coalescent events between times 0 and  $t$ . The intervals  $I_{i,k}$  are defined by the sampling and coalescent times, so the number of active lineages, denoted  $l_{i,k}$ , in an interval is constant. For  $k = 2, \dots, n$ , the intervals that end in a coalescent event are denoted  $I_{0,k} = (\max\{t_k, s_j\}, t_{k-1}]$ , for  $s_j < t_{k-1}$ , and intervals that end with a sampling event are denoted  $I_{i,k} = (\max\{t_k, s_{j+1}\}, s_{j+i-1}]$ , for  $t_k < s_{j+i-1} \leq s_j < t_{k-1}$  with  $i > 0$ .

Coalescent models are continuous-time Markov chains used to model a genealogy from a sample of sequences (Kingman, 1982). Rodrigo et al. (1999) extended coalescent theory for heterochronous sampling to calculate the joint distribution of a genealogy given its sampling times, number of samples collected at each time, and the effective population size, as the product of conditional densities and tail probabilities of coalescent times (Rodrigo and Felsenstein, 1999):

$$\begin{aligned} P(\mathbf{g}|\mathbf{s}, \mathbf{n}, N_e(t)) &= \prod_{k=2}^n P(t_{k-1}|t_k, \mathbf{s}, N_e(t)) \\ &= \prod_{k=2}^n \frac{A_{0,k}}{N_e(t_{k-1})} \exp\left\{-\int_{I_{0,k}} \frac{A_{0,k}}{N_e(t)} dt - \sum_{i \geq 1} \int_{I_{i,k}} \frac{A_{i,k}}{N_e(t)} dt\right\}, \end{aligned} \tag{1}$$

with the coalescent factors  $A_{i,k} = \binom{l_{i,k}}{2}$ .

Assuming the effective population size trajectory  $N_e(t)$  is an unknown function in continuous time, the integral in Eq 1 is intractable. We adopt a common approach (Palacios and Minin, 2012; Gill et al., 2013; Faulkner et al., 2020), well described by Lan et al. (2015), that discretizes the effective population size to be piecewise constant on a regular grid,  $\mathbf{x} = \{x_d\}_{d=1}^D$ , spanning from the most recent sampling time,  $s_m = x_1$ , to the first coalescent time,  $t_1 = x_D$  (Lan et al., 2015). In this approach we define  $N_e(t) = \exp[\gamma(t)]$ , and approximate  $N_e(t)$  by  $N_e^\gamma(t) = \sum_{d=1}^{D-1} \exp(\gamma_d) 1_{t \in (x_d, x_{d+1}]}$ .

The  $\gamma_d$ 's *a priori* follow a first order random walk:  $\gamma_d|\gamma_{d-1} \sim N(\gamma_{d-1}, 1/\kappa)$  with  $\gamma_1 \sim N(0, \sigma_\gamma^2)$ . We adopt the common approach of using a gamma prior distribution for the hyperparameter  $\kappa$ .

With heterochronous sampling, it is likely that the frequency of sampling is related to the number of infections in the population (e.g., increased sampling intensity when there is an increase in infections). Additional factors may also influence the sampling intensity, such as time variable cost of sequencing a pathogen genome. In the preferential sampling model, we model sampling events as a Poisson Process with intensity  $\lambda(t)$  that depends on such time-varying factors:

$$\log \lambda(t) = \beta_0 + \beta_1 \log[N_e(t)] + \beta_2 f_2(t) + \dots + \beta_p f_p(t), \quad (2)$$

where  $f_2, \dots, f_m(t)$  are the additional time-varying covariates (Karcher et al., 2020). Note the sampling intensity can include interactions between the covariates and the log effective population size, but we do not include them in our model here. The coefficients  $\boldsymbol{\beta} = (\beta_0, \beta_1, \dots, \beta_p)$ 's are assigned independent normal priors with means  $\boldsymbol{\mu}_\beta$  and variances  $\boldsymbol{\sigma}_\beta$ . Since the effective population size is piecewise constant on the regular grid  $\boldsymbol{x}$ , for simplicity we require time-varying covariates also be piecewise constant on the same grid.

Altogether, the posterior we are interested in is

$$\begin{aligned} Pr(\boldsymbol{g}, \boldsymbol{\gamma}, \kappa, \boldsymbol{\beta}, \boldsymbol{\theta} | \boldsymbol{y}, \boldsymbol{s}) \propto & Pr(\boldsymbol{y} | \boldsymbol{g}, \boldsymbol{\theta}) Pr(\boldsymbol{g} | \boldsymbol{\gamma}, \boldsymbol{s}) Pr(\boldsymbol{s} | \boldsymbol{\gamma}, \boldsymbol{\beta}) Pr(\boldsymbol{\gamma} | \kappa) \\ & Pr(\boldsymbol{\theta}) Pr(\kappa) Pr(\boldsymbol{\beta}). \end{aligned} \quad (3)$$

Approximation of this posterior via Markov Chain Monte Carlo (MCMC) is implemented in the phylodynamic software BEAST (Suchard et al., 2018; Karcher et al., 2020). This Bayesian inference is time and memory intensive though, so it is common in practice to estimate the genealogy first and assume the genealogy is known. When the genealogy is known the posterior of interest reduces to

$$Pr(\boldsymbol{\gamma}, \kappa, \boldsymbol{\beta} | \boldsymbol{g}, \boldsymbol{s}) \propto Pr(\boldsymbol{g} | \boldsymbol{\gamma}, \boldsymbol{s}) Pr(\boldsymbol{s} | \boldsymbol{\gamma}, \boldsymbol{\beta}) Pr(\boldsymbol{\gamma} | \kappa) Pr(\kappa) Pr(\boldsymbol{\beta}). \quad (4)$$

Approximations of this posterior via MCMC and via Integrated Nested Laplace Approximations (INLA) (Palacios and Minin, 2012) are implemented in the phylodynamic R package `phylodyn` (Karcher et al., 2017).

## 2.2 Accounting for reporting delays

The time delay between collecting a sample and depositing that sample's sequence into a database arose as a problem during the SARS-CoV-2 pandemic, because of the urgent need for up-to-date understanding of disease dynamics. Missing the most recent data is especially problematic for the preferential sampling model because of the dependency between the sampling intensity and the effective population size. Intuitively, a model that takes into account preferential sampling would underestimate the effective population size close to the present time due to the lack of observed samples. One possible solution of this problem is to use a coalescent model without the preferential sampling component, avoiding the dependency between the sampling intensity and the effective population size. While the biases from the missing data would be avoided with this strategy, unaccounted preferential sampling can result in biases, and wider credible intervals than those modeled with preferential sampling (Karcher et al., 2016).

Another way to circumvent this missing data issue is to only use data up to a time when all of the data is likely to have been reported (e.g., data up to two months prior to time of analysis). For example, phylodynamics was used to compare SARS-CoV-2 lineages in England with data truncated by two weeks to avoid reporting delays in 2021 (Volz et al., 2021). The major pitfall of this truncation strategy is the inability to perform real-time phylodynamics to inform outbreak mitigation, a problem that increases for locations or time periods with extensive reporting delays.

## 2.3 Incorporating reporting delay distribution into preferential sampling model

To mitigate effects of reporting delays on real-time phylodynamic analyses with preferential sampling, we propose incorporating information about the distribution of recent delays in the sampling intensity model. In the preferential sampling model sampling times are modeled as a Poisson process with intensity  $\lambda(t)$ . Let  $r(t)$  be the probability that a sample collected at time  $t$  was sequenced and reported by the time of the analysis. Define the observed sampling times,  $\tilde{\mathbf{s}}$  to be the subset of the true sampling times,  $\mathbf{s}$ , that are reported by the time of analysis. Then the observed sampling intensity,  $\tilde{\lambda}(t)$ , could be expressed as the product of the true sampling intensity and the probability of a sample being reported, resulting in a thinned Poisson process with intensity  $\tilde{\lambda}(t) = \lambda(t)r(t)$ . Plugging Eq 2 into the definition of  $\tilde{\lambda}(t)$ , we get the following new model for the log-sampling intensity

$$\log \tilde{\lambda}(t) = \log[r(t)] + \beta_0 + \beta_1 \log[N_e(t)] + \beta_2 f_2(t) + \dots + \beta_p f_p(t). \quad (5)$$

## 2.4 Implementation of reporting delay aware preferential sampling model

We developed a new version of **phylodyn** (Karcher et al., 2017), **phylodyn2** (<https://github.com/CatalinaMedina/phylodyn2>), which has a well-documented subset of the functionality of **phylodyn**, with the additional ability to account for reporting delays in real-time analyses by implementing our proposed reporting delay aware preferential sampling model. In this implementation, the reporting probabilities are assumed to be known. The empirical cumulative distribution of recent reporting delays is used to calculate the reporting probabilities,  $\mathbf{r} = (r_1, r_2, \dots, r_D)$ . Similarly to the effective population size and any covariates, the reporting probabilities  $\mathbf{r}$  are also defined as piecewise constant across the regular grid  $\mathbf{x}$ .

The R package **phylodyn** included several posterior sampling strategies. For **phylodyn2** we chose to focus on the INLA based strategy to approximate the marginal posterior distributions  $Pr(\gamma_i|\mathbf{g})$ . This INLA implementation formulates the model for sampling times as a Poisson regression. However, the original **phylodyn** implementation did not allow for inclusion of a user specified offset term into this regression. In **phylodyn2** we added an offset term to the original Poisson regression, where this offset term is set to  $\log[r(t)]$ , calculated from a user specified vector of recent reporting delays.

One could view the  $\log[r(t)]$  term as a time-varying covariate of the sampling intensity, with coefficient one. The appeal of this perspective is the ease of use for phylodynamic tools that allow for time-varying covariates in the sampling intensity, such as BEAST and **phylodyn**. One could specify  $\log[r(t)]$  as a regression covariate with a narrow prior for the coefficient of this term centered at one. This adds unnecessary randomness, since the coefficient of this term is theoretically one, but the ease of use makes this option worth exploring. This implementation is also available in **phylodyn2**, and its performance is examined in the supplementary materials.

All code to reproduce the results in this paper can be found at <https://github.com/CatalinaMedina/reporting-delays-in-phylodynamics-paper>.

# 3 Results

## 3.1 Simulations

We performed simulation studies to mimic real-time phylodynamic analyses in the presence of preferential sampling, aiming at two primary objectives. Firstly, to investigate the effects of reporting delays with currently available phylodynamic inferential strategies. Secondly, to compare the performance of our proposed model against the currently available strategies. Of key interest is how well the effective population size trajectory can be inferred close to the most recent sampling time.

Three real-time inferential strategies were considered for comparison: avoid modeling the sampling time dependency by using the the Bayesian nonparametric phylodynamic reconstruction (BNPR) model, model the sampling time dependency with the Bayesian nonparametric phylodynamic reconstruction with preferential sampling (BNPR PS) model, and model the sampling time dependency and reporting delays with our proposed reporting delay aware preferential sampling model. We also fit the BNPR PS model to all of the data, regardless of whether it was reported, to provide a retrospective baseline for the performance of these real-time inferential strategies.

We used three simulation scenarios with the same effective population size trajectory, but across different time periods so that the effects of reporting delays with different trajectory behavior near time zero could be investigated. The upper-left panel of Fig 2 shows the effective population size trajectory, as well as the most recent sampling time, the time of analysis, for each scenario. Since time is viewed in reverse, the most recent sample in simulation scenario C is time zero, and the earliest sample was 300 days prior. Scenarios A and B had sampling time periods of 150 days and 220 days, respectively. Scenario A is meant to resemble an initial outbreak, which would have fewest samples due to reporting delays. Scenario B allows us to examine behavior when there is an increase occurring near present time, but less sampling. Lastly, in scenario C there is a decline near present time and the recent peak corresponds to more reported samples near time zero than scenario B.

Sampling times were simulated from an inhomogeneous Poisson process with intensity  $\lambda(t) = \exp(\beta_0)[N_e(t)]^{\beta_1}$ . Coalescent times were simulated using a time-transformation technique where the coalescent likelihood is treated as an inhomogeneous Poisson process (Slatkin and Hudson, 1991). Parameter  $\beta_1$  was set to 2 to create a reasonably strong preferential sampling effect and  $\exp(\beta_0)$  was selected to achieve a sample size of approximately 1500 samples, each with its own sampling time.

For each sampling time we simulated a random Bernoulli to indicate if a sample was reported by the time of analysis. Sampling times for each scenario are plotted in Fig 2 and colored by whether it was observed or not. To create realistic delays, the reporting probabilities were obtained from the empirical reporting delay distribution of SARS-CoV-2 sequences collected in the state of Washington. See the real data investigation results subsection for details, visualized in upper-right panel of Fig 2. The tips of the genealogy of the full tree that correspond to unreported samples were pruned from the tree, to get the observed genealogy. Each inference was performed with the INLA-based Bayesian phylodynamic inference implemented in the R package `phylodyn2`.

We will begin by discussing the results of a single simulation within a scenario, in order to better understand the patterns in the performance of each inference strategy across all of the simulations. Fig 3 plots the true (solid lines) and inferred (dashed lines) effective population size trajectory for the 100 days prior to the most recently collected sample. Here we focus on the two options of real-time inference, the BNPR and BNPR PS models, and our proposed inclusion of reporting probabilities in the BNPR PS model. While the ultimate goal is to be able to infer the true effective population size trajectory, it is useful to see how closely the data generating model can approximate the true trajectory, within simulation scenario C, where the trajectory of interest is on the decline at present time. This is why each plot also contains the BNPR PS inference performed retrospectively on all of the data, not just the observed data – this serves as a baseline to compare the inference of  $N_e(t)$  from each real-time inferential method. The white background indicates the time period of interest, where delays are probable, and conversely the gray background indicates the period where reporting delays are unlikely. We chose to use the 90th percentile of the Washington state data reporting delays distribution, which was 41 days in this case, as the cutoff for these two periods.

In the first panel of Fig 3 we see real-time inference with the BNPR model, which ignores the dependency between  $N_e(t)$  and the sampling time. The BNPR model appears to have relatively low bias, but wide 95% credible intervals that increase in width near time zero. The real-time inference with the BNPR PS model stands out because of the bias which increases as time approaches the most recently collected sample. This demonstrates the bias introduced when using the data

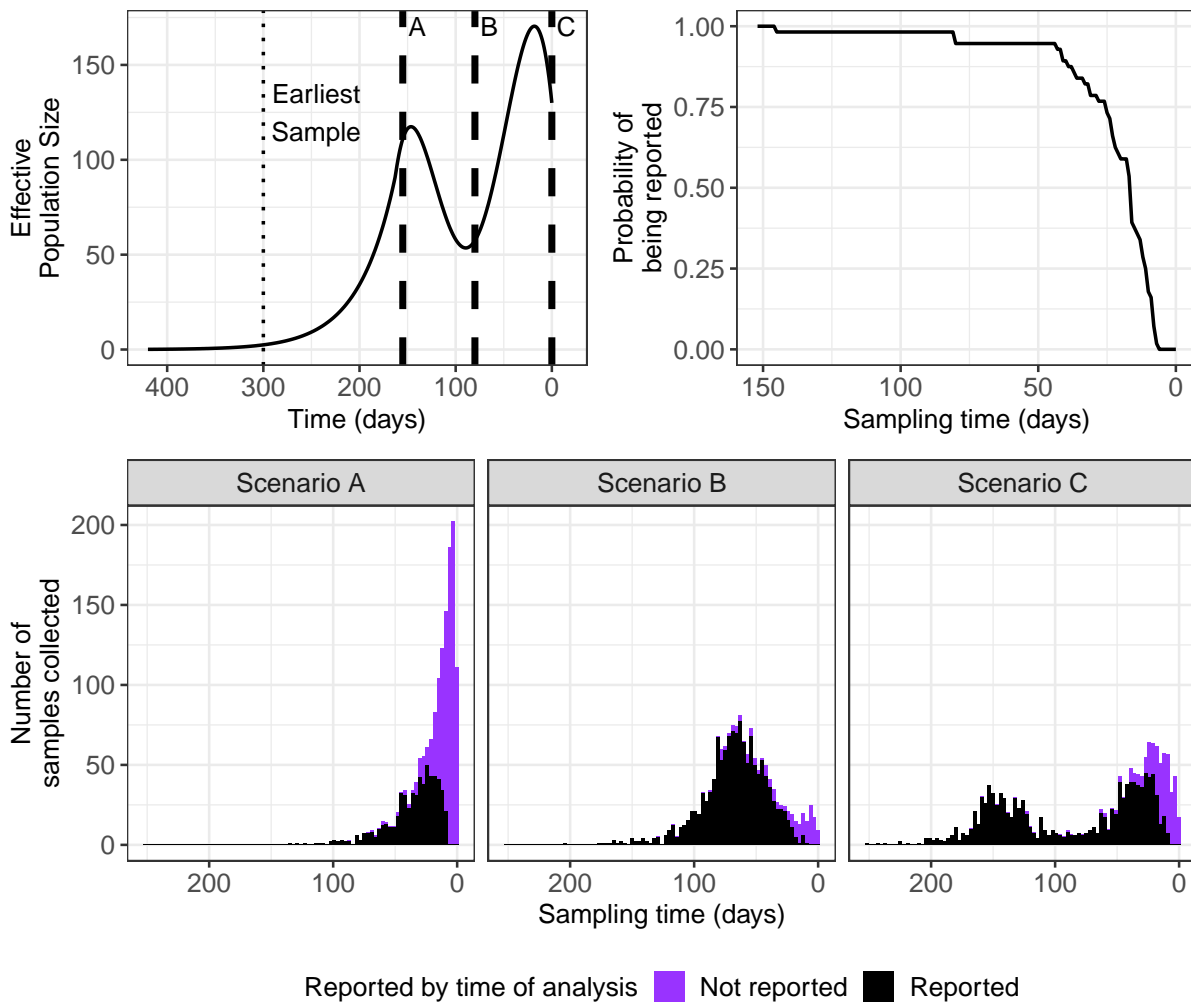


Figure 2: Simulation details: effective population trajectories (upper left plot), reporting probability by sampling time (upper right plot) obtained from the Washington state data, and histograms of sampling times from the last simulation of in each simulation scenario, approximately 1500 samples each, colored by whether sample was reported by time of analysis (bottom plots). Each simulation scenario had a different time zero, i.e., time of latest sample (dashed lines). The earliest sampling time in each scenario was at the same point in the trajectory (dotted line).



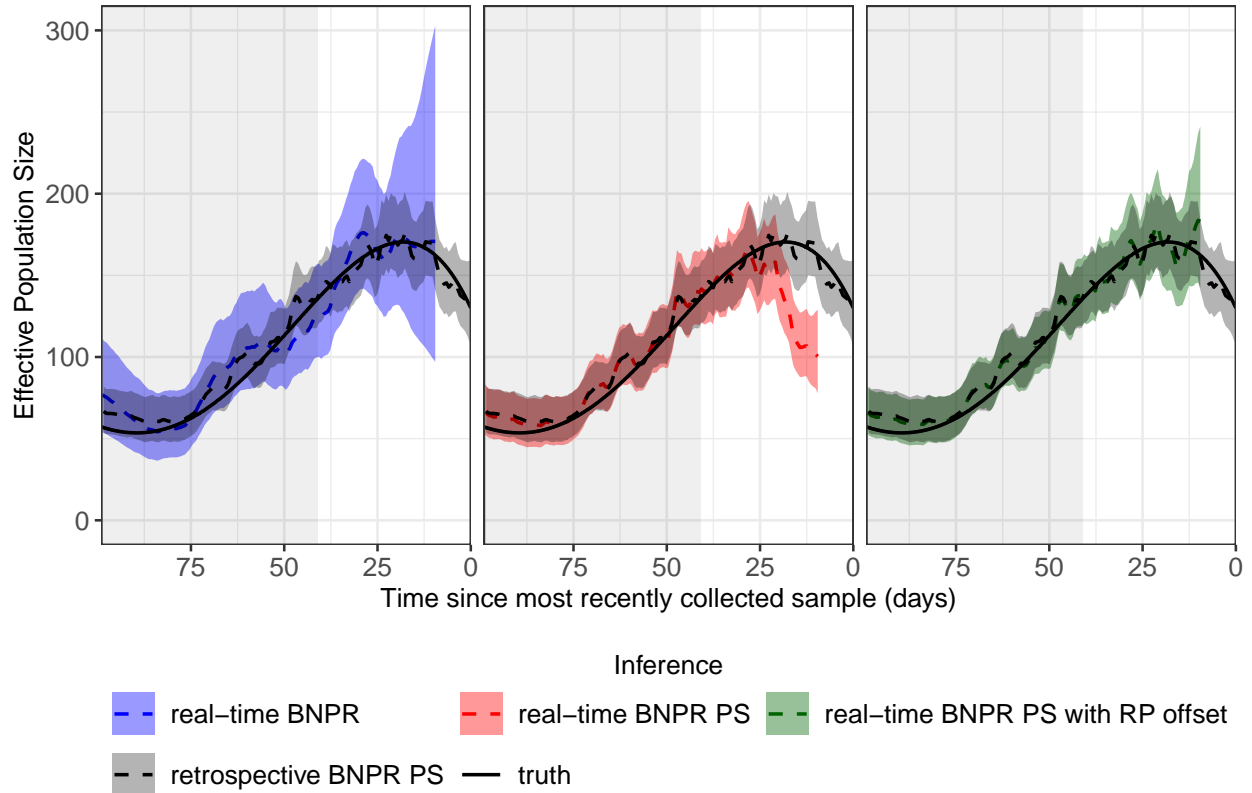


Figure 3: Comparison of real-time phylodynamic methods to infer the effective population size trajectory for a single simulation in scenario C, with reporting delays and preferential sampling present. Median estimates of the effective population size and 95% credible intervals are plotted. The white background indicates the recent time period likely suffering from reporting delays, specifically where reporting probabilities (RPs) are below 90%, and is therefore the region of interest.

generating model, the BNPR PS model, when there are reporting delays present in the data. Alternatively, our implementation of the BNPR PS model with the reporting probabilities included as an offset in the sampling intensity, has less bias than the BNPR PS model near time zero and visibly narrower 95% credible intervals than the BNPR model near time zero.

The results identified from the single simulation in Fig 3 generally persist across all 500 simulations, in each of the three simulation scenarios, visualized in Fig 4. The plots present a seven-day moving average of the mean relative deviation, mean percent of 95% Bayesian credible intervals which covered the true value, and mean 95% credible interval width for each inference strategy in each simulation scenario. A moving average was chosen because a metric of the inference over the entire time period would be insufficient to describe how inference performance changes with proximity to time zero. Mean relative deviation is the most important of the three chosen metrics because it assess accuracy, of the point estimate, interval coverage was selected to examine the accuracy of the uncertainty of the estimates, and interval width was useful for assessing precision to compare those models with good accuracy and good coverage. Since the performance of these estimation strategies near time zero is of key interest, these plots were truncated to the most recent 100 days. To view the performance metrics results for all inferential methods considered see the supplemental material Table S1, Table S2, and Table S3.

Focusing on the time period of interest, the most recent 41 days, our proposed reporting delays aware BNPR PS model consistently has lower mean relative deviation than the BNPR method, in each seven-day moving average, though there is not much practical difference. The BNPR PS model has increasing relatively large mean relative deviation as sampling times decrease to time zero, in each simulation scenario. The absolute maximum mean relative deviations in scenario A are all achieved in the week prior to time zero are 0.15, 0.82, and 0.06 for the BNPR, BNPR PS, and our reporting delay aware model respectively. The 95% Bayesian credible intervals for the BNPR and our reporting delays aware BNPR PS model are consistently conservative, while the BNPR PS model’s 95% credible intervals’ coverage drops below 95% and approaches 0% as sampling time approaches time zero. Finally, while maintaining competitively low bias and high coverage, our proposed model consistently has lower mean 95% Bayesian credible interval widths than the BNPR model, with the difference between the two models increasing as sampling time approaches time zero.

### 3.2 Real data investigation: Washington state COVID dynamics

We used SARS-CoV-2 sequences from Washington state for the purpose of investigating the differences between a real-time phylodynamic analysis with and without our proposed method to account for reporting delays in genomic data. The SARS-CoV-2 sequences were accessed via the GISAID database available at [https://gisaid.org/EPI\\_SET\\_220330me](https://gisaid.org/EPI_SET_220330me), for Washington state sampled between February 01, 2021 and August 01, 2021, inclusive (Shu and McCauley, 2017). This time period was of interest because researchers were regularly sequencing Washington samples at this point in the pandemic, and the reporting behavior is relatively consistent during this period. Fig 5 plots seven day averages of the number of COVID-19 cases per 100,000 people in population in the state of Washington, the daily number of SARS-CoV-2 samples available in GISAID for Washington, colored by whether the sequence was sampled by August 01, 2021 (left plot), and the empirical cumulative distribution function for sampling dates between July 01, 2021 and August 01, 2021.

The observed data are samples that had been sequenced and reported to GISAID on or before August 01, 2021, time zero of our analysis. The 90th percentile of the reporting delays distribution is 41 days. Since we are interested in the inference of  $N_e(t)$  when reporting delays are present, we chose to focus our attention on the most recent 41 days.

Genealogy estimation was performed in BEAST for each data set: the full 500 sequences, observed 412 sequences, and 375 remaining sequences after truncation. We used the HKY substitution model with empirically estimated base frequencies (Hasegawa et al., 1985), Bayesian Skygrid co-

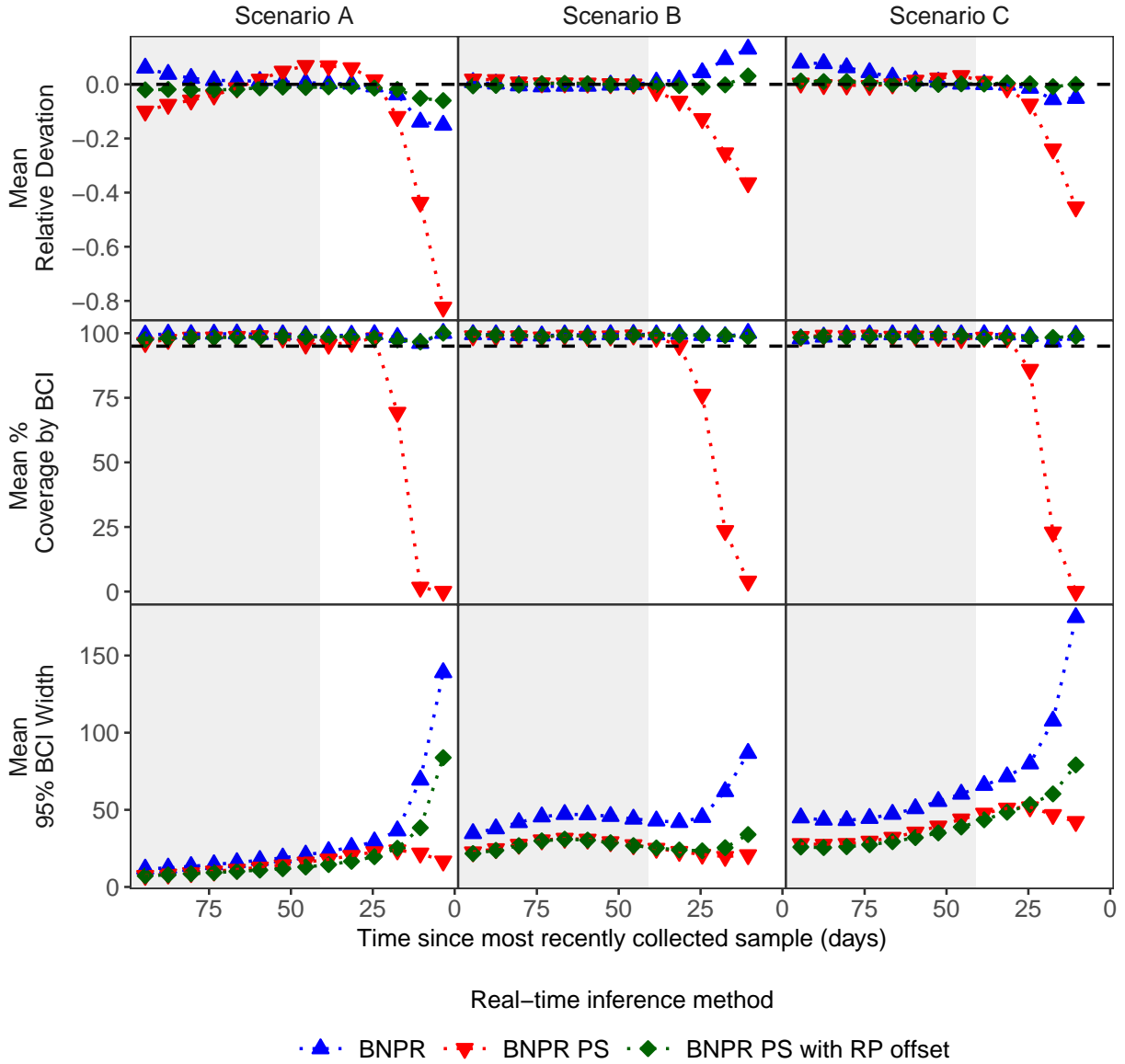


Figure 4: Seven-day moving averages of the mean relative deviation, mean percent coverage, and mean interval width by the 95% Bayesian credible intervals, for each real-time phylodynamic strategies to infer the effective population size in each simulation scenario with preferential sampling (PS) and reporting delays in the observed data. Inference was performed with Bayesian nonparametric phylodynamic reconstruction (BNPR), BNPR PS, and with BNPR PS with reporting probabilities (RP) in sampling intensity as an offset.

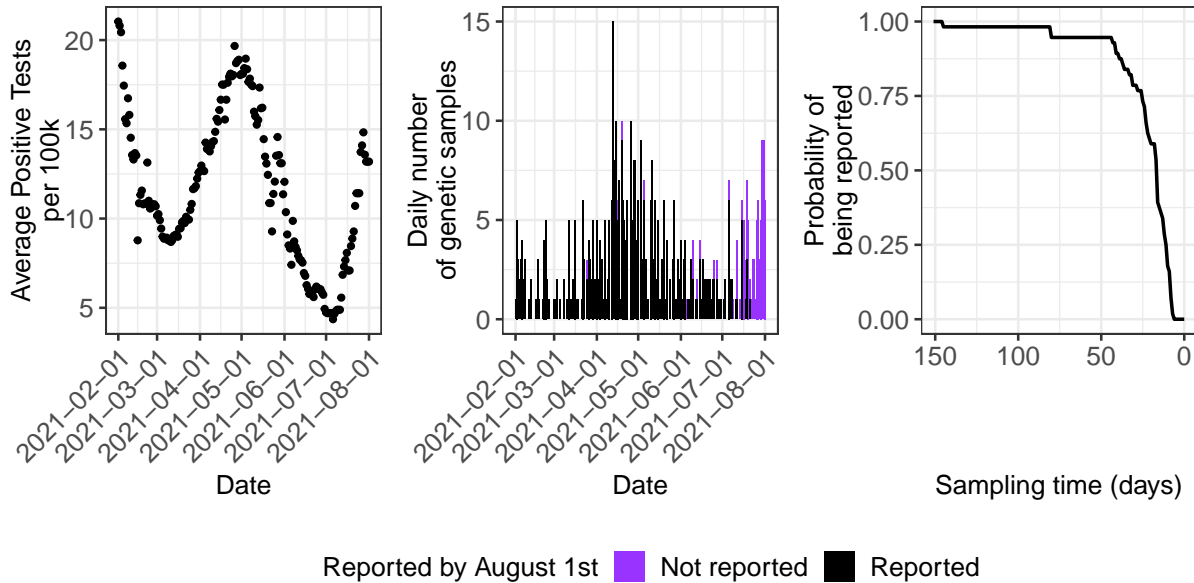


Figure 5: Left plot is the average number of positive COVID-19 tests for most recent seven days per 100,000 people in the state of Washington. Middle panel shows number of SARS-CoV-2 genetic samples collected in Washington state, colored by whether the sample was reported by the time of analysis, August 1, 2021. Right panel shows empirical cumulative distribution of reporting delays from the month prior to time of analysis.

alescent model (Gill et al., 2013; Drummond et al., 2002), and a Uniform prior on the clock rate between  $2.38 \times 10^{-3}$  and  $8 \times 10^{-4}$  (Neher, 2022). The MCMC was run for  $25 \times 10^6$  iterations, logging parameters every 2000th iteration. The maximum clade credibility tree of the posteriors were used as the known genealogy in the phylodynamic reconstruction, for each of the three analyses. See the supplemental materials section for more details about this analysis to obtain the genealogies.

Inference of the effective population size was performed with the same strategies used in our simulations to compare the performance of our proposed methods against available options. Fig 6 shows the inference of the effective population size for three modeling strategy: Bayesian nonparametric phylodynamic reconstruction (BNPR), BNPR with preferential sampling (BNPR PS), and our proposed inclusion of reporting probabilities in the BNPR PS model as an offset.

The retrospective analysis with all of the collected samples with the BNPR PS model infers a peak in transmission activity in mid April of 2021, dropping to a minimum in mid June, followed by a steady increase continuing into August 2021. The results for these analyses are consistent with the trajectory of COVID-19 cases for this time period, visualized in Fig 5, with approximately a two week delay which could be due to reporting delays in COVID test results.

When comparing the real-time analyses we see similar patterns as those identified in our simulations. Using the retrospective BNPR PS model for comparison we see near real time, the BNPR model suffers from low precision, the BNPR PS model’s credible intervals disagree with the retrospective analysis credible intervals, and our proposed BNPR PS with the reporting probability correction is consistent with the retrospective BNPR PS model results, with higher precision than the BNPR model. This gain in precision found with our proposed model would have allowed real-time analysis to infer the increase near present time that the two currently available competitive methods underestimated.

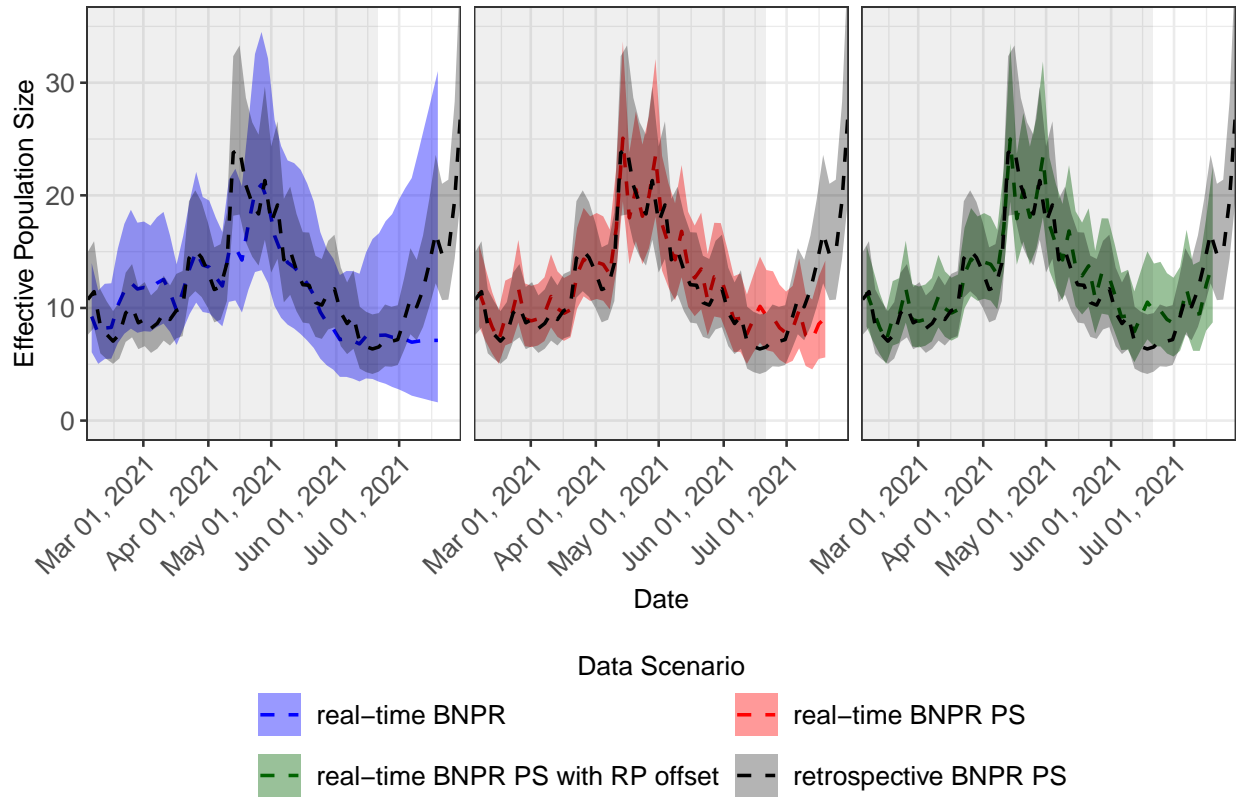


Figure 6: Bayesian nonparametric phylodynamic reconstruction (BNPR) methods used to infer effective population size trajectory for SARS-CoV-19 in Washington state. Each panel shows the inference from a real-time analysis on data suffering from reporting delays and from a retrospective analysis with completely reported data. The white background indicates the recent time period likely suffering from reporting delays.

## 4 Discussion

In this work we investigated the effects of reporting delays on real-time phylodynamic methods to infer the effective population size and we proposed a reporting delay aware model. Through simulations we demonstrated that when preferential sampling is present, real-time analysis with the BNPR PS model suffers from increasingly extreme bias when inferring the effective population size near present time, implying that the BNPR PS model should not be used for such cases because it is unreliable. We also showed that when the preferential sampling relationship is not modeled, real-time analysis with the BNPR model has less bias than the BNPR PS model, but is largely uninformative due to its low precision near present time. Across simulations we found our reporting delay aware model to performed comparably to the BNPR model, not suffering from the same biases as the BNPR PS model, and with increased data our model obtains increased precision near present time, relative to the BNPR model. Our results support the intuition that we can infer  $N_e(t)$  more accurately and precisely with more data, specifically when there are more samples sequenced and available for analysis. Beyond the simulations, our Washington data analysis found evidence of preferential sampling and behavior consistent with our simulation results: we saw agreeable results between our reporting delay aware model and the retrospective BNPR PS model, the real-time BNPR model had very low precision near present time, and the real-time BNPR PS model strongly disagreed with the retrospective BNPR PS model. The simulated and real data results provide compelling arguments that reporting delays should not be ignored in real-time analysis, and that the effective population size trajectory is a reasonable indicator for the effective number of infections.

For simplicity, we assumed the pathogen genealogy is known in our implementation of the reporting delay aware model in `phylodyn2`, obtaining the marginal posteriors of  $N_e(t)$  with INLA. The value of this choice is that it is fast and can handle much larger number of sequences than BEAST which jointly infers the genealogy and other model parameters, including  $N_e(t)$ . Computational speed and feasibility are necessary considerations with Bayesian phylodynamic methods, especially with online surveillance. A natural next step from this work would be to incorporate our reporting probability adjustment into the joint posterior inferred by the BNPR PS model in BEAST.

Our reporting delay aware model currently assumes that reporting probabilities are known, and our implementation uses recent reporting delays to estimate current reporting probabilities. This strategy is limited to locations, times, lineages, and even laboratories where there is believed to be consistency in reporting delays for sequences (Petroni et al., 2023). As such, care is necessary when defining the reporting probability distribution for use in the sampling intensity of our model. The next extension of this work would be to jointly infer the reporting probabilities and the effective population size. This could allow for increased accuracy and better reflect our uncertainty about reporting probabilities, especially for areas with rapid changes in reporting behavior. Perhaps of most interest would be to allow for the reporting delay distribution to change overtime, allowing for updated surveillance of the effective population size with continual data collection.

The BNPR PS method models the sampling intensity parametrically, so naturally there may be concern of model misspecification, especially when studying new variants of unknown infectiousness. Cappello and Palacios (2022) proposed a model which allows for the relationship between the effective population size and the sampling intensity to vary with time as follows:  $\lambda(t) = \beta(t)N_e(t)$ , where  $\beta(t)$  is inferred nonparametrically from the genetic and sampling time data (Cappello and Palacios, 2022). It would be of interest to extend this model to incorporate known reporting probabilities. The next question would be if it could jointly infer reporting probabilities and  $N_e(t)$  with the time-varying  $\beta(t)$ .

Our proposed reporting delay aware model is a first step in mitigating the effects of reporting delays on real-time phylodynamic analyses. This work has important implications for real-time research with genomic data. We identified that the data generating model can be biased when

ignoring the presence of missing data near present time due to reporting delays. The severity of this bias increases as the number of sequences observed decreases, but this bias can be corrected by using historical data about reporting delays.

## 5 Acknowledgements

We gratefully acknowledge all data contributors, i.e., the authors and their originating laboratories responsible for obtaining the specimens, and their submitting laboratories for generating the genetic sequence and metadata and sharing via the GISAID Initiative, on which this research is based.

This work was in part funded by the UC Irvine Investing to Develop Center-Scale Multidisciplinary Convergence Research Programs Seed Funding Award and by the UC CDPH Modeling Consortium. Julia Palacios acknowledges support from NSF grant DMS-2143242, NIH grant R35GM14833801. We thank Lorenzo Cappello for useful discussions during the early stages of this project.

## References

- Bastos, L. S., Economou, T., Gomes, M. F. C., Villela, D. A. M., Coelho, F. C., Cruz, O. G., Stoner, O., Bailey, T., and Codeço, C. T. (2019). A modelling approach for correcting reporting delays in disease surveillance data. *Statistics in Medicine* **38**, 4363–4377.
- Billenstein, R. J. and Höhna, S. (2024). Comparison of Bayesian Coalescent Skyline Plot Models for Inferring Demographic Histories. *Molecular Biology and Evolution* **41**, msae073.
- Cappello, L. and Palacios, J. A. (2022). Adaptive preferential sampling in phylodynamics with an application to SARS-CoV-2. *Journal of Computational and Graphical Statistics* **31**, 541–552.
- Cori, A. and Kucharski, A. (2024). Inference of epidemic dynamics in the COVID-19 era and beyond. *OSF Preprints*.
- Drummond, A. J., Nicholls, G. K., Rodrigo, A. G., and Solomon, W. (2002). Estimating mutation parameters, population history and genealogy simultaneously from temporally spaced sequence data. *Genetics* **161**, 1307–1320.
- Drummond, A. J., Rambaut, A., Shapiro, B., and Pybus, O. G. (2005). Bayesian coalescent inference of past population dynamics from molecular sequences. *Molecular Biology and Evolution* **22**, 1185–1192.
- Engebretsen, S., Diz-Lois Palomares, A., Rø, G., Kristoffersen, A. B., Lindstrøm, J. C., Engø-Monsen, K., Kaminen, M., Hin Chan, L. Y., Dale, Ø., Midtbø, J. E., Stenerud, K. L., Ruscio, F. D., White, R., Frigessi, A., and Blasio, B. F. d. (2023). A real-time regional model for COVID-19: Probabilistic situational awareness and forecasting. *PLOS Computational Biology* **19**, e1010860. Publisher: Public Library of Science.
- Faulkner, J. R., Magee, A. F., Shapiro, B., and Minin, V. N. (2020). Horseshoe-based Bayesian nonparametric estimation of effective population size trajectories. *Biometrics* **76**, 677–690.
- Felsenstein, J. (1981). Evolutionary trees from DNA sequences: A maximum likelihood approach. *Journal of Molecular Evolution* **17**, 368–376.
- Fountain-Jones, N. M., Appaw, R. C., Carver, S., Didelot, X., Volz, E., and Charleston, M. (2020). Emerging phylogenetic structure of the SARS-CoV-2 pandemic. *Virus Evolution* **6**, veaa082. PMID: 33335743 PMCID: PMC7717445.

- Frost, S. D. W. and Volz, E. M. (2010). Viral phylodynamics and the search for an ‘effective number of infections’. *Philosophical Transactions of the Royal Society B: Biological Sciences* **365**, 1879–1890. Publisher: Royal Society.
- Gill, M. S., Lemey, P., Faria, N. R., Rambaut, A., Shapiro, B., and Suchard, M. A. (2013). Improving Bayesian population dynamics inference: A coalescent-based model for multiple loci. *Molecular Biology and Evolution* **30**, 713–724.
- Hasegawa, M., Kishino, H., and Yano, T.-a. (1985). Dating of the human-ape splitting by a molecular clock of mitochondrial DNA. *Journal of Molecular Evolution* **22**, 160–174.
- Kalia, K., Saberwal, G., and Sharma, G. (2021). The lag in SARS-CoV-2 genome submissions to gisaid. *Nature Biotechnology* **39**, 1058–1060. Number: 9 Publisher: Nature Publishing Group.
- Karcher, M. D., Carvalho, L. M., Suchard, M. A., Dudas, G., and Minin, V. N. (2020). Estimating effective population size changes from preferentially sampled genetic sequences. *PLOS Computational Biology* **16**, e1007774. Publisher: Public Library of Science.
- Karcher, M. D., Palacios, J. A., Bedford, T., Suchard, M. A., and Minin, V. N. (2016). Quantifying and mitigating the effect of preferential sampling on phylodynamic inference. *PLOS Computational Biology* **12**, e1004789. Publisher: Public Library of Science.
- Karcher, M. D., Palacios, J. A., Lan, S., and Minin, V. N. (2017). phylodyn: an R package for phylodynamic simulation and inference. *Molecular Ecology Resources* **17**, 96–100.
- Kingman, J. F. C. (1982). The coalescent. *Stochastic Processes and their Applications* **13**, 235–248.
- Lan, S., Palacios, J. A., Karcher, M., Minin, V. N., and Shahbaba, B. (2015). An efficient Bayesian inference framework for coalescent-based nonparametric phylodynamics. *Bioinformatics* **31**, 3282–3289.
- Neher, R. A. (2022). Contributions of adaptation and purifying selection to SARS-CoV-2 evolution. *Virus Evolution* **8**, veac113.
- Palacios, J. A. and Minin, V. N. (2012). Integrated nested Laplace approximation for Bayesian nonparametric phylodynamics. In *Proceedings of the Twenty-Eighth Conference on Uncertainty in Artificial Intelligence*, UAI’12, page 726–735, Arlington, Virginia, USA. AUAI Press.
- Petrone, M. E., Lucas, C., Menasche, B., Breban, M. I., Yildirim, I., Campbell, M., Omer, S. B., Holmes, E. C., Ko, A. I., Grubaugh, N. D., Iwasaki, A., Wilen, C. B., Vogels, C. B. F., and Fauver, J. R. (2023). Nonsystematic reporting biases of the SARS-CoV-2 variant mu could impact our understanding of the epidemiological dynamics of emerging variants. *Genome Biology and Evolution* **15**, evad052. PMID: 36974986 PMCID: PMC10113931.
- Pybus, O. G., Rambaut, A., and Harvey, P. H. (2000). An integrated framework for the inference of viral population history from reconstructed genealogies. *Genetics* **155**, 1429–1437.
- Rich, S. N., Richards, V., Mavian, C., Magalis, B. R., Grubaugh, N., Rasmussen, S. A., Dellicour, S., Vrancken, B., Carrington, C., Fisk-Hoffman, R., Danso-Odei, D., Chacreton, D., Shapiro, J., Seraphin, M. N., Hepp, C., Black, A., Dennis, A., Trovão, N., Vandamme, A.-M., Rasmussen, A., Lauzardo, M., Dean, N., Salemi, M., and Prospero, M. (2023). Application of phylodynamic tools to inform the public health response to COVID-19: qualitative analysis of expert opinions. *JMIR Formative Research* **7**, e39409.
- Rodrigo, A. G. and Felsenstein, J. (1999). Coalescent approaches to HIV population genetics. *The evolution of HIV* pages 233–272.



- Shu, Y. and McCauley, J. (2017). GISAID: Global initiative on sharing all influenza data – from vision to reality. *Eurosurveillance* **22**, 30494. Publisher: European Centre for Disease Prevention and Control.
- Slatkin, M. and Hudson, R. R. (1991). Pairwise comparisons of mitochondrial DNA sequences in stable and exponentially growing populations. *Genetics* **129**, 555–562.
- Strimmer, K. and Pybus, O. G. (2001). Exploring the demographic history of DNA sequences using the generalized skyline plot. *Molecular Biology and Evolution* **18**, 2298–2305.
- Suchard, M. A., Lemey, P., Baele, G., Ayres, D. L., Drummond, A. J., and Rambaut, A. (2018). Bayesian phylogenetic and phylodynamic data integration using beast 1.10. *Virus Evolution* **4**, vey016.
- van Ballegooijen, W. M., van Houdt, R., Bruisten, S. M., Boot, H. J., Coutinho, R. A., and Wallinga, J. (2009). Molecular sequence data of hepatitis b virus and genetic diversity after vaccination. *American Journal of Epidemiology* **170**, 1455–1463. PMID: 19910379.
- Volz, E., Mishra, S., Chand, M., Barrett, J. C., Johnson, R., Geidelberg, L., Hinsley, W. R., Laydon, D. J., Dabrera, G., O’Toole, Á., Amato, R., Ragonnet-Cronin, M., Harrison, I., Jackson, B., Ariani, C. V., Boyd, O., Loman, N. J., McCrone, J. T., Gonçalves, S., Jorgensen, D., Myers, R., Hill, V., Jackson, D. K., Gaythorpe, K., Groves, N., Sillitoe, J., Kwiatkowski, D. P., Flaxman, S., Ratmann, O., Bhatt, S., Hopkins, S., Gandy, A., Rambaut, A., and Ferguson, N. M. (2021). Assessing transmissibility of SARS-CoV-2 lineage B.1.1.7 in England. *Nature* **593**, 266–269. Number: 7858 Publisher: Nature Publishing Group.
- Volz, E. M., Kosakovsky Pond, S. L., Ward, M. J., Leigh Brown, A. J., and Frost, S. D. W. (2009). Phylodynamics of infectious disease epidemics. *Genetics* **183**, 1421–1430.

# Supplementary Materials

## S-1 Simulation results

In the manuscript we focused on three real-time inferential strategies: BNPR, BNPR PS, and our proposed reporting delay aware BNPR PS model with reporting probabilities incorporated as an offset in the model of the sampling intensity. For completeness, we also considered the truncation technique, where only samples collected up until some point in time are used. This is meant to avoid the most recent time period, and therefore avoid reporting delays in data, but by definition is not much of a real-time analysis. Regardless, we investigated this strategy to show that the truncation technique can result in important recent behavior remaining unknown.

We also considered an alternative implementation of our reporting delay aware preferential sampling model. This alternative implementation is discussed in the last subsection of our methods section in the manuscript. The implementation with reporting probabilities being incorporated as an offset is useful because any existing software that can incorporate a time varying covariate into the log sampling intensity equation would be automatically able to implement our proposed model. As expected, this implementation performed similarly to our originally proposed implementation, with the caveat of increased variation due to the need to model the coefficient of this regression term, which is known to be one in theory.

We also additionally consider the BNPR model used retrospectively on all data. We included this because, while the BNPR PS model is the data generating model in this case, it is less commonly used than the BNPR model. An important finding is that the real-time inference with our proposed reporting delay aware BNPR PS model on only reported samples is competitive with the retrospective BNPR model fit to all of the data, further supporting why our model should be used.

## S-1.1 Further simulation results with Washington state's reporting delays

### S-1.1.1 Results from last simulation in each scenario

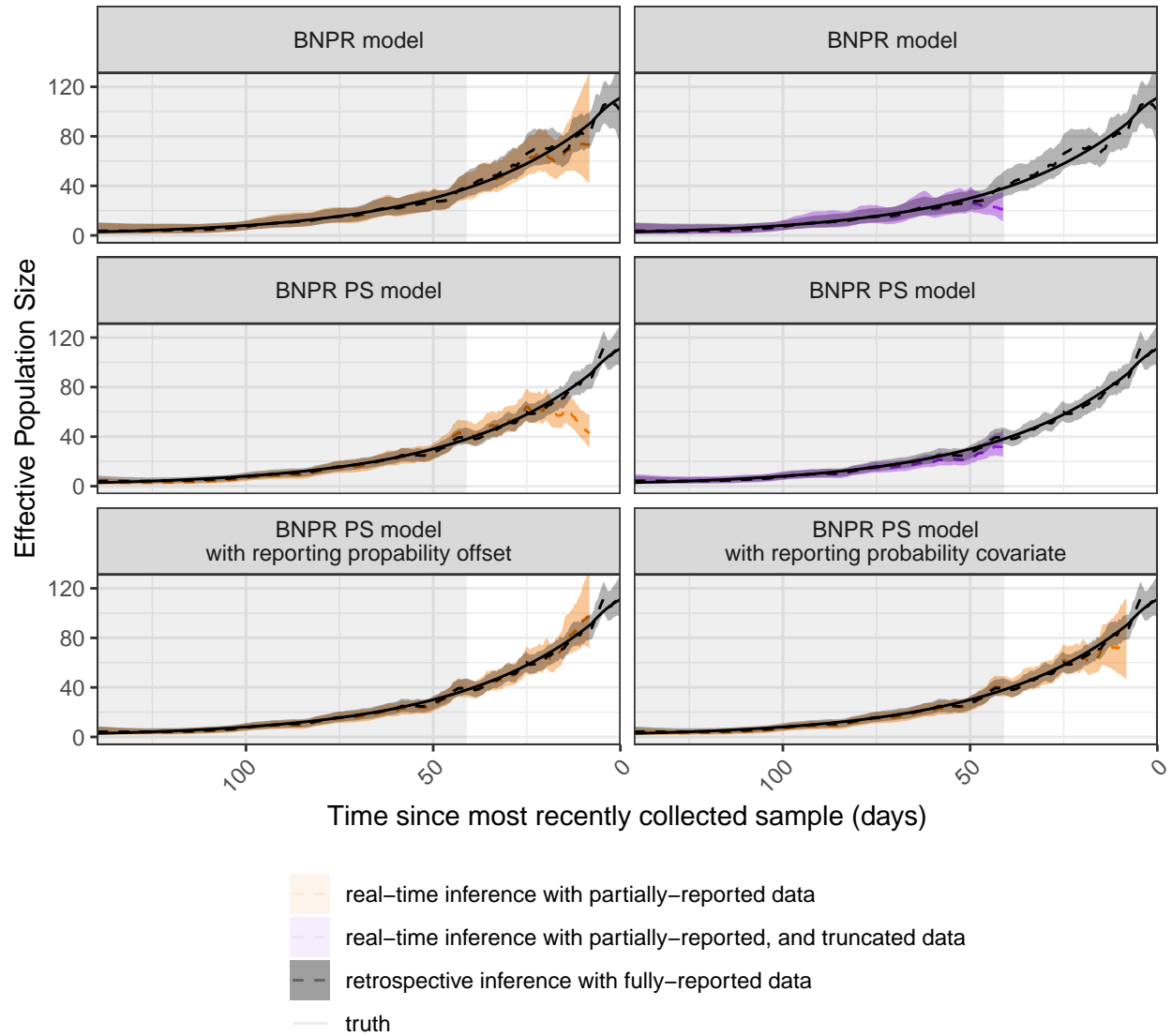


Figure S-1: Comparison of phylodynamic estimation methods of effective population size trajectory for three different simulated data scenarios from the scenario A trajectory.

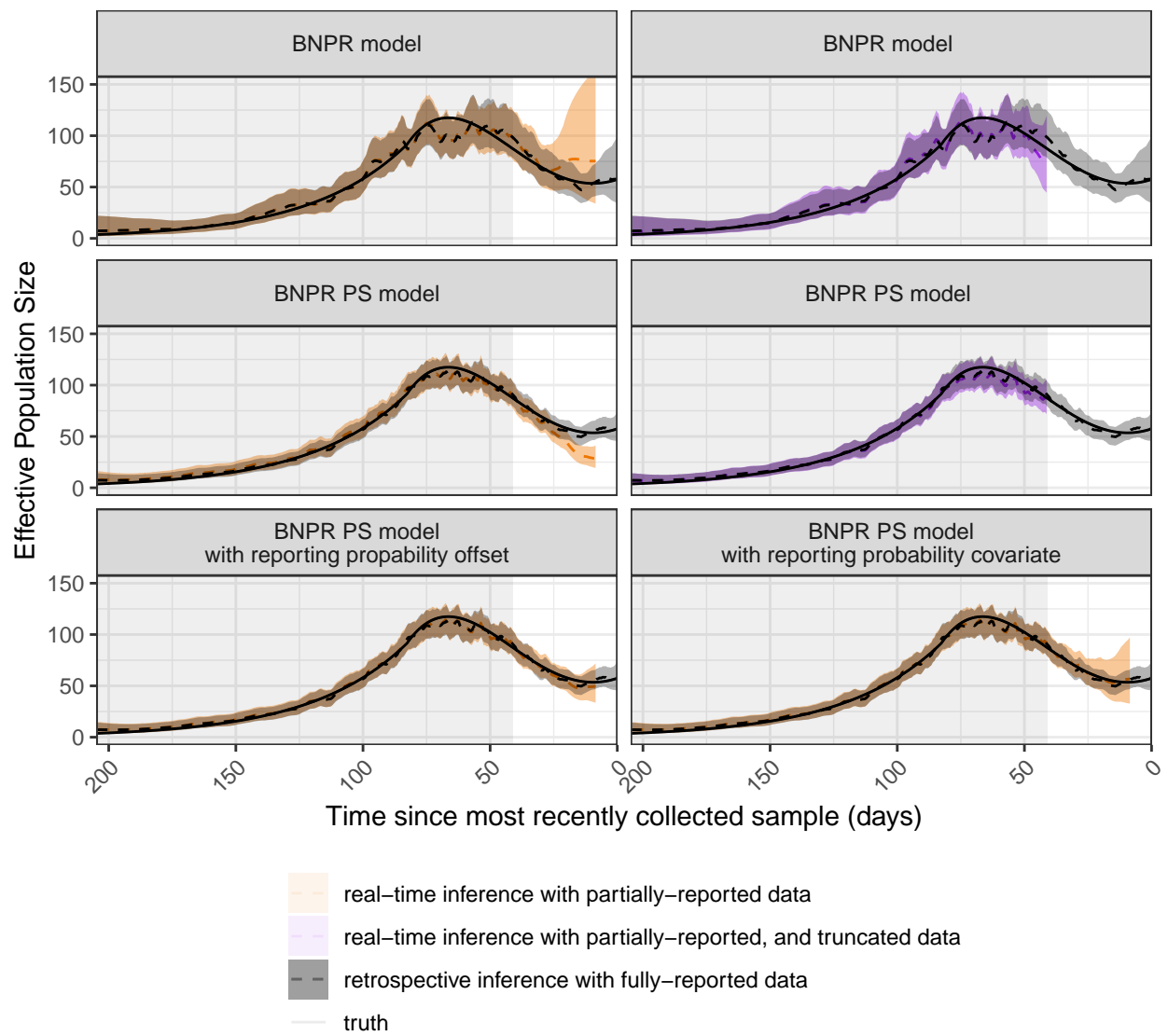


Figure S-2: Comparison of phylodynamic estimation methods of effective population size trajectory for three different simulated data scenarios from the scenario B trajectory.

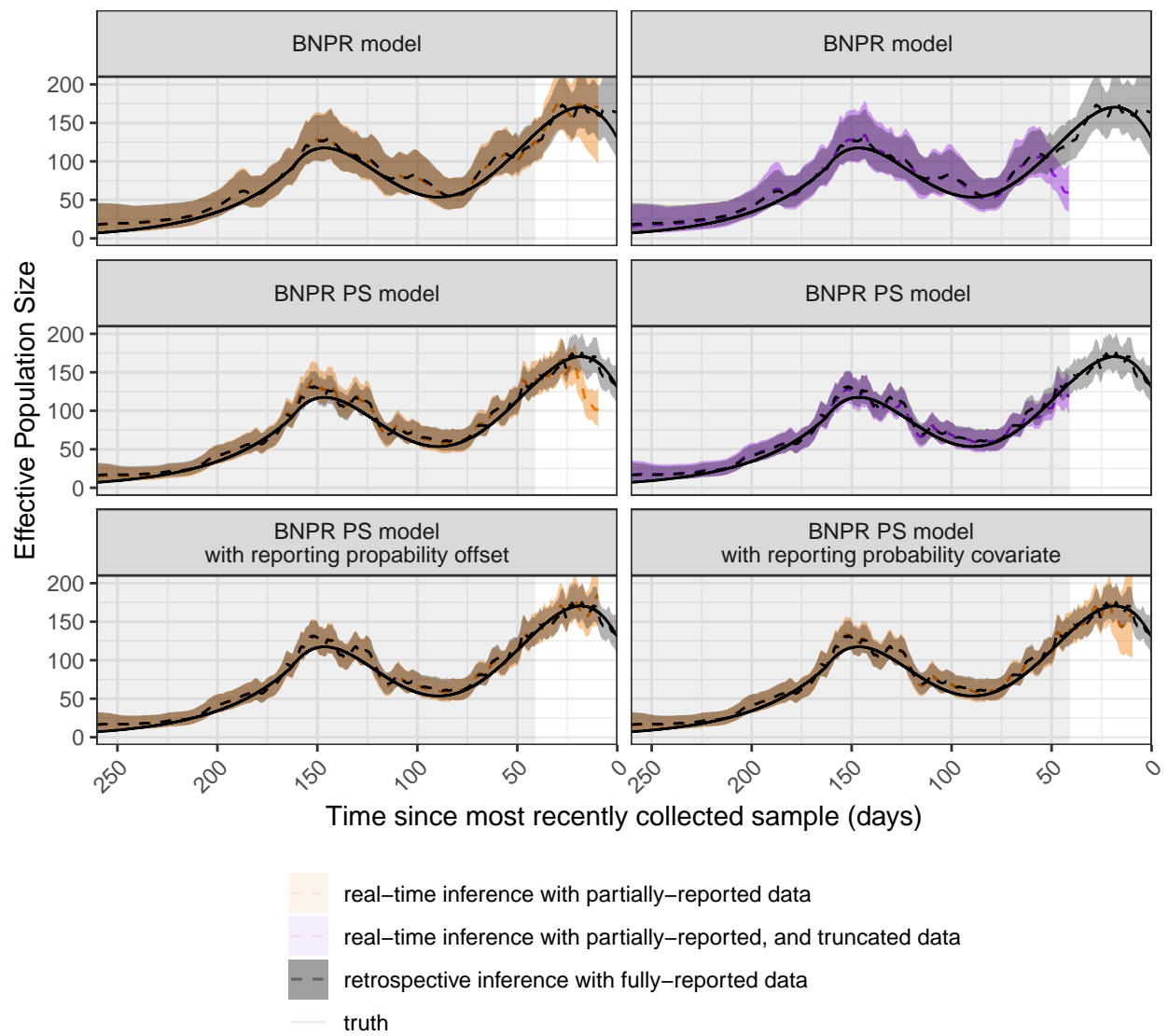


Figure S-3: Comparison of phylodynamic estimation methods of effective population size trajectory for three different simulated data scenarios from the scenario C trajectory.

### S-1.1.2 Performance metrics across all simulations

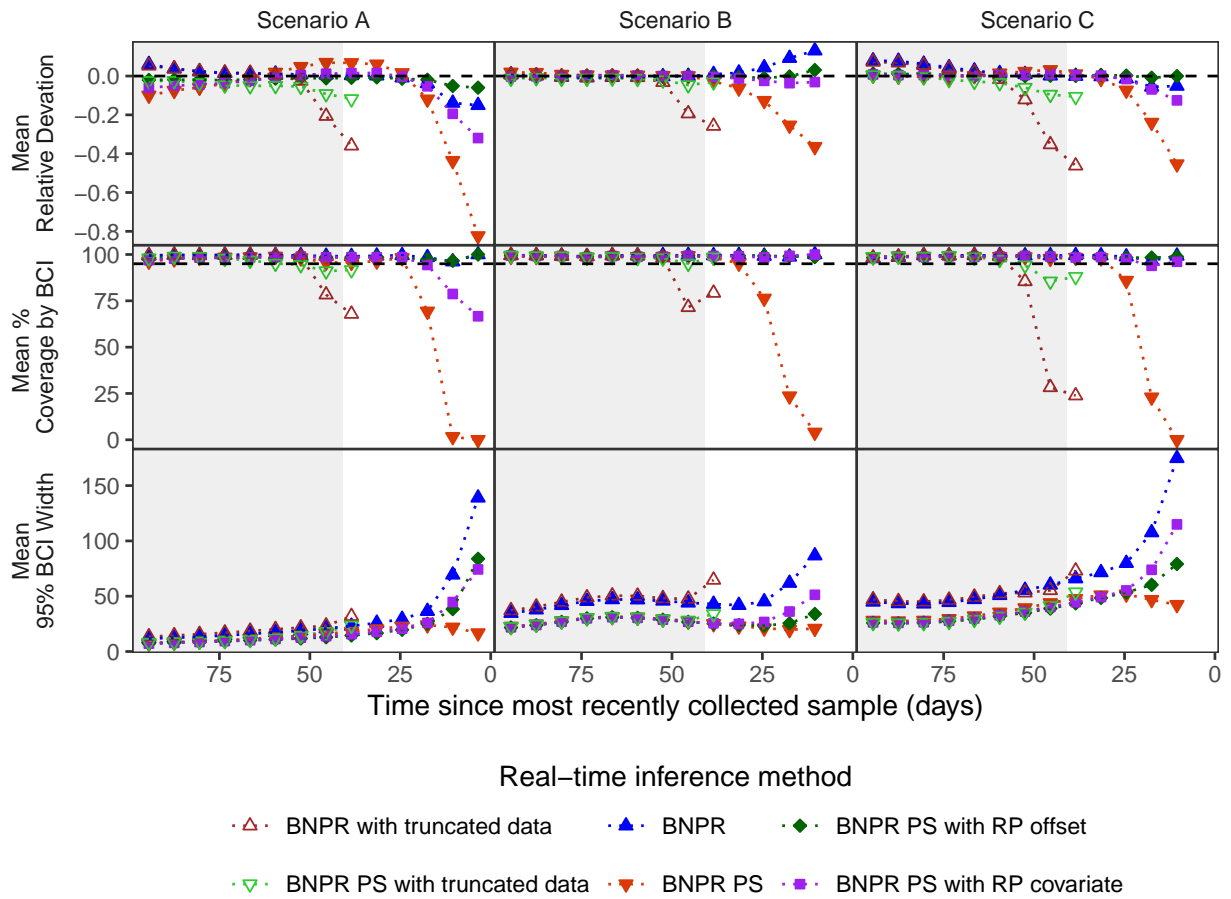


Figure S-4: Seven-day moving averages of the mean relative deviation, mean percent coverage, and mean interval width by the 95% Bayesian credible intervals, for each real-time phylodynamic strategies to infer the effective population size in each simulation scenario with preferential sampling (PS) and reporting delays in the observed data. Inference was performed with Bayesian nonparametric phylodynamic reconstruction (BNPR), BNPR PS, and with BNPR PS with reporting probabilities (RP) in sampling intensity as an offset.

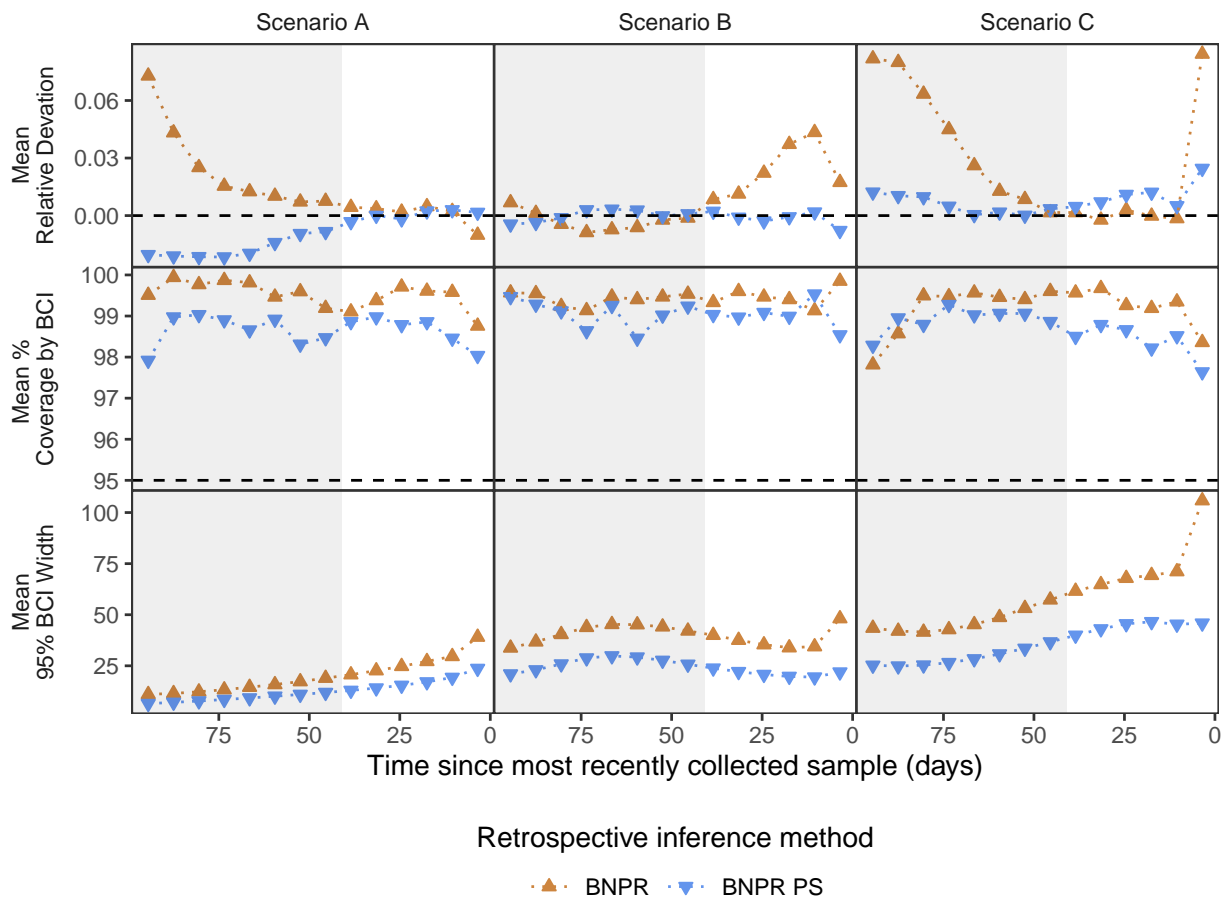


Figure S-5: Seven-day moving averages of the mean relative deviation, mean percent coverage, and mean interval width by the 95% Bayesian credible intervals, for each retrospective phylodynamic strategy to infer the effective population size in each simulation scenario with preferential sampling (PS) and no reporting delays in the observed data. Inference was performed with Bayesian nonparametric phylodynamic reconstruction (BNPR) and BNPR PS.

Table S-1: Mean relative deviation of all inferential techniques for effective population size in each data scenario for 500 simulations in scenarios A, B, and C. Time periods span approximately from first simulated sampling time to 90th percentile of historic reporting delays, 41 days. The final time period for each simulation scenario spans from the first to last sampling time simulated.

Time period (days)	Retrospective		Real-time inference					
	BNPR	BNPR PS	Trunc. BNPR	Tunc. BNPR PS	BNPR	BNPR PS	BNPR PS with RP offset	BNPR PS with RP covariate
<b>Scenario A</b>								
[0,7)	-0.01	0.00			-0.15	-0.82	-0.06	-0.32
[7,14)	0.00	0.00			-0.14	-0.44	-0.05	-0.19
[14,21)	0.00	0.00			-0.04	-0.12	-0.02	-0.05
[21,28)	0.00	0.00			-0.01	0.02	-0.01	0.00
[28,35)	0.00	0.00			0.00	0.06	-0.01	0.02
[35,42)	0.00	0.00	-0.36	-0.12	0.00	0.07	-0.01	0.01
[0,154]	0.12	0.05	0.10	0.05	0.10	-0.02	0.05	0.01
<b>Scenario B</b>								
[7,14)	0.04	0.00			0.13	-0.36	0.03	-0.03
[14,21)	0.04	0.00			0.09	-0.25	0.00	-0.04
[21,28)	0.02	0.00			0.04	-0.13	-0.01	-0.02
[28,35)	0.01	0.00			0.02	-0.06	0.00	-0.01
[35,42)	0.01	0.00	-0.26	-0.03	0.01	-0.03	0.00	0.00
[0,228]	0.14	0.07	0.12	0.06	0.14	0.07	0.06	0.06
<b>Scenario C</b>								
[7,14)	0.00	0.01			-0.05	-0.45	0.00	-0.13
[14,21)	0.00	0.01			-0.06	-0.24	-0.01	-0.07
[21,28)	0.00	0.01			-0.01	-0.07	0.00	-0.02
[28,35)	0.00	0.01			0.00	-0.01	0.01	0.00
[35,42)	0.00	0.00	-0.46	-0.11	0.00	0.01	0.00	0.00
[0,307]	0.14	0.08	0.12	0.08	0.13	0.04	0.08	0.06



Table S-2: Percent of 95 percent Bayesian credible intervals that covered the true effective population size, from all inferential techniques in each data scenario for 500 simulations in scenarios A, B, and C. Time periods span approximately from first simulated sampling time to 90th percentil of historic reporting delays, 41 days. The final time period for each simulation scenario spans from the first to last sampling time simulated.

Time period (days)	Retrospective		Real-time inference					
	BNPR	BNPR PS	Trunc. BNPR	Tunc. BNPR PS	BNPR	BNPR PS	BNPR PS with RP offset	BNPR PS with RP covariate
<b>Scenario A</b>								
[0,7)	98.76	98.04			100.00	0.00	100.00	66.67
[7,14)	99.58	98.46			96.13	1.62	96.59	78.69
[14,21)	99.61	98.86			98.44	69.31	97.42	94.37
[21,28)	99.71	98.79			99.52	98.14	98.10	98.52
[28,35)	99.38	98.98			99.28	96.37	98.69	98.55
[35,42)	99.10	98.86	67.90	91.65	99.03	95.64	98.58	98.57
[0,154]	98.75	96.79	97.21	95.84	98.71	90.96	96.71	96.32
<b>Scenario B</b>								
[7,14)	99.13	99.53			100.00	3.98	98.62	99.95
[14,21)	99.40	98.99			98.75	23.54	99.07	99.24
[21,28)	99.47	99.08			99.19	76.29	99.24	98.40
[28,35)	99.60	98.97			99.62	95.20	99.25	99.08
[35,42)	99.33	99.03	79.24	98.40	99.45	98.39	99.19	99.18
[0,228]	98.06	96.21	97.14	96.20	98.21	89.79	96.53	96.49
<b>Scenario C</b>								
[7,14)	99.35	98.52			99.24	0.00	98.76	96.10
[14,21)	99.19	98.22			96.71	22.96	98.34	93.92
[21,28)	99.26	98.66			98.83	85.93	98.30	97.53
[28,35)	99.67	98.79			99.40	98.11	98.51	98.56
[35,42)	99.57	98.50	23.85	87.97	99.51	98.36	98.23	98.34
[0,307]	97.60	95.89	95.36	94.39	97.95	92.67	96.00	96.30

Table S-3: Mean width of 95 percent Bayesian credible intervals of effective population size from all inferential techniques in each data scenario for 500 simulations in scenarios A, B, and C. Time periods span approximately from first simulated sampling time to 90th percentile of historic reporting delays, 41 days. The final time period for each simulation scenario spans from the first to last sampling time simulated.

Time period (days)	Retrospective		Real-time inference					
	BNPR	BNPR PS	Trunc. BNPR	Tunc. BNPR PS	BNPR	BNPR PS	BNPR PS with RP offset	BNPR PS with RP covariate
<b>Scenario A</b>								
[0,7)	39.06	23.68			138.99	16.69	83.81	74.24
[7,14)	29.61	19.29			69.37	21.83	38.36	44.73
[14,21)	27.18	17.09			36.48	23.90	25.08	25.85
[21,28)	24.75	15.41			29.31	22.69	19.60	20.60
[28,35)	22.63	14.10			25.77	20.27	16.60	17.88
[35,42)	20.67	12.95	31.91	23.54	23.06	17.94	14.50	15.69
[0,154]	17.74	10.73	16.35	10.00	20.21	12.57	12.37	13.00
<b>Scenario B</b>								
[7,14)	34.39	19.47			86.69	20.78	33.97	51.30
[14,21)	33.87	19.78			61.89	19.65	25.46	36.15
[21,28)	35.36	20.72			45.16	21.07	23.40	26.70
[28,35)	37.55	22.12			41.90	22.89	23.98	24.98
[35,42)	39.98	23.83	64.73	33.94	42.89	24.92	25.28	25.56
[0,228]	30.83	18.40	31.57	18.66	33.77	19.48	19.54	20.67
<b>Scenario C</b>								
[7,14)	71.12	45.30			174.69	42.27	79.11	114.94
[14,21)	69.30	46.56			107.61	46.78	60.30	73.87
[21,28)	67.87	45.53			79.86	51.78	53.39	55.21
[28,35)	64.83	43.03			71.50	50.95	48.45	49.27
[35,42)	61.57	39.92	73.03	53.62	65.93	47.69	43.52	44.63
[0,307]	47.19	28.39	45.18	27.16	50.51	31.19	30.12	31.94

Boxplot of posterior median of preferential sampling coefficient, by estimation strategy and simulation scenario

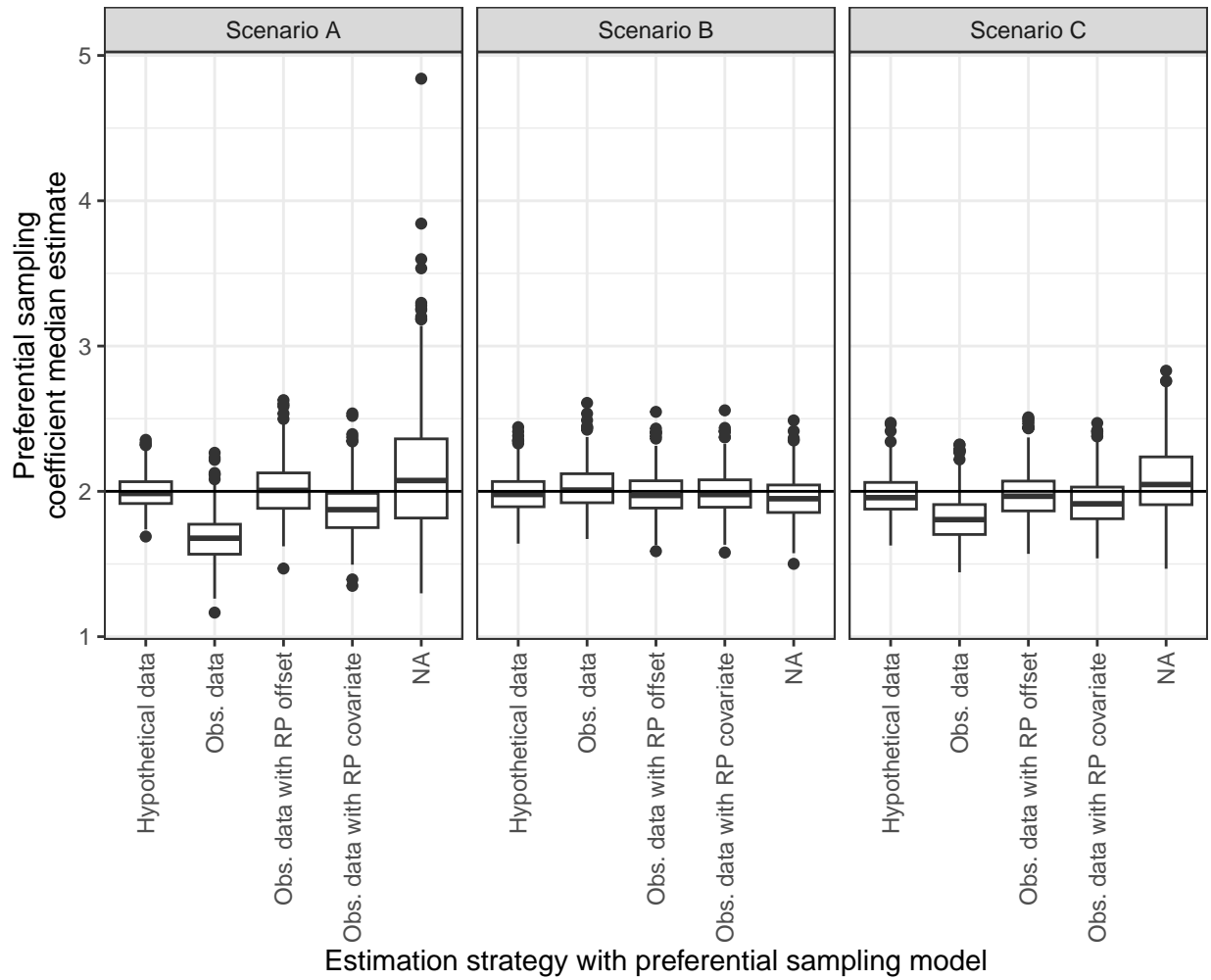


Figure S-6: Median preferential sampling coefficient estimate from simulations by estimation strategy and simulation scenario.

## S-1.2 Simulation with Santa Clara County reporting delays (more extreme delays than Washington state)

All simulation details are identical to the simulations in the main manuscript, with a difference in reporting probabilities. Here we use the empirical reporting delays of Santa Clara County as the reporting probabilities. The 90th percentile of reporting delays is 54 for Santa Clara County, while Washington state's was 41. Since these delays are more extreme this serves to help investigate how more extreme delays affect the analysis.

### S-1.2.1 Results from last simulation in each scenario

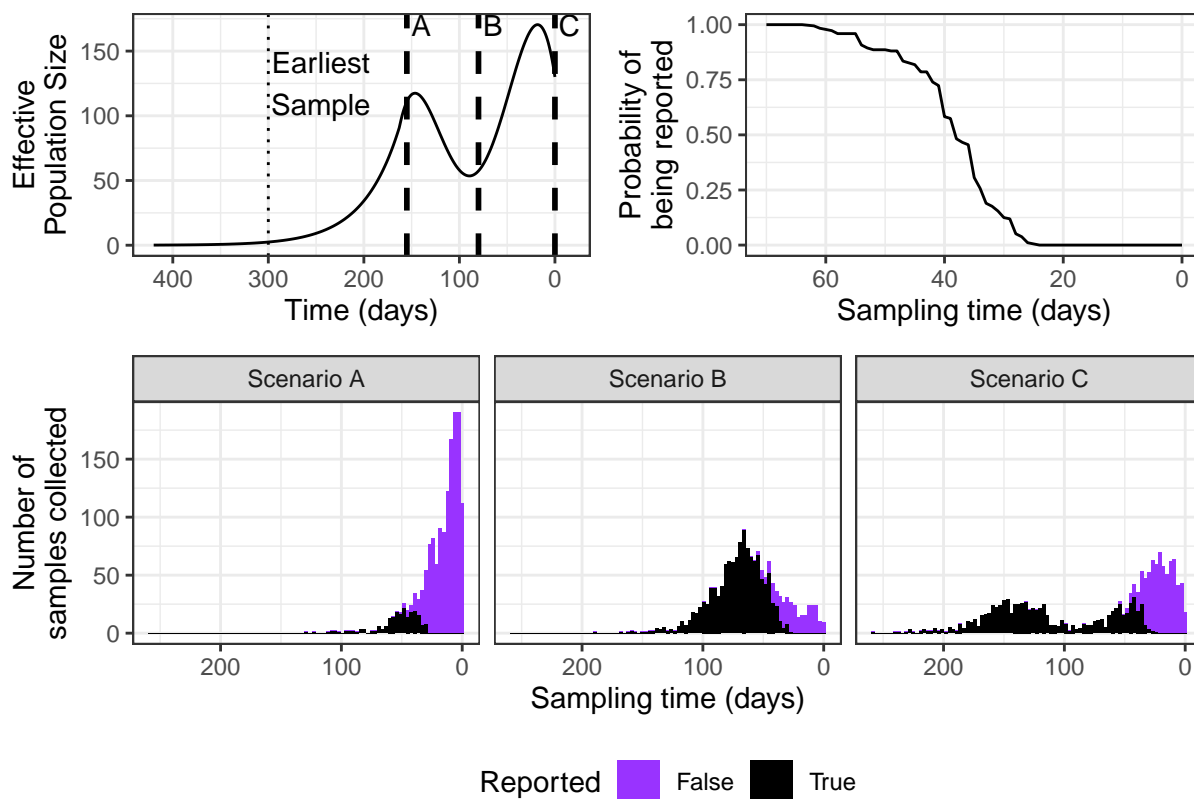


Figure S-7: Three panel plot providing simulation details: effective population trajectories (upper left plot), reporting probability by sampling time (upper right plot) obtained from Santa Clara County empirical cumulative distribution, and histograms of sampling times from the last simulation of in each simulation scenario colored by whether sample was reported by time of analysis (bottom plots). Each simulation scenario had a different time zero, i.e. time of latest sample (dashed lines). The earliest sampling time in each scenario was at the same point in the trajectory (dotted line).

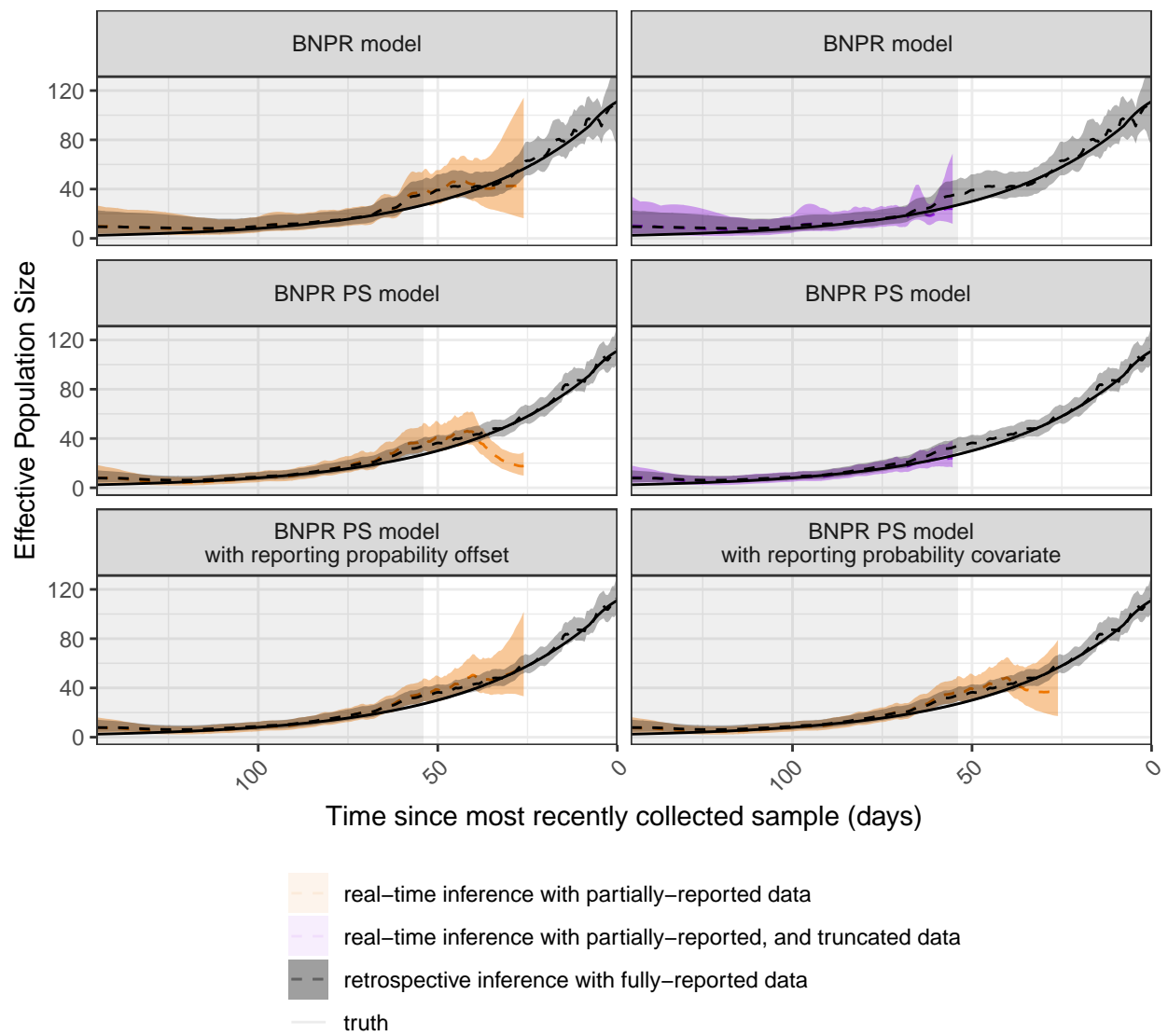


Figure S-8: Comparison of phylodynamic estimation methods of effective population size trajectory for three different simulated data scenarios from the scenario A trajectory.

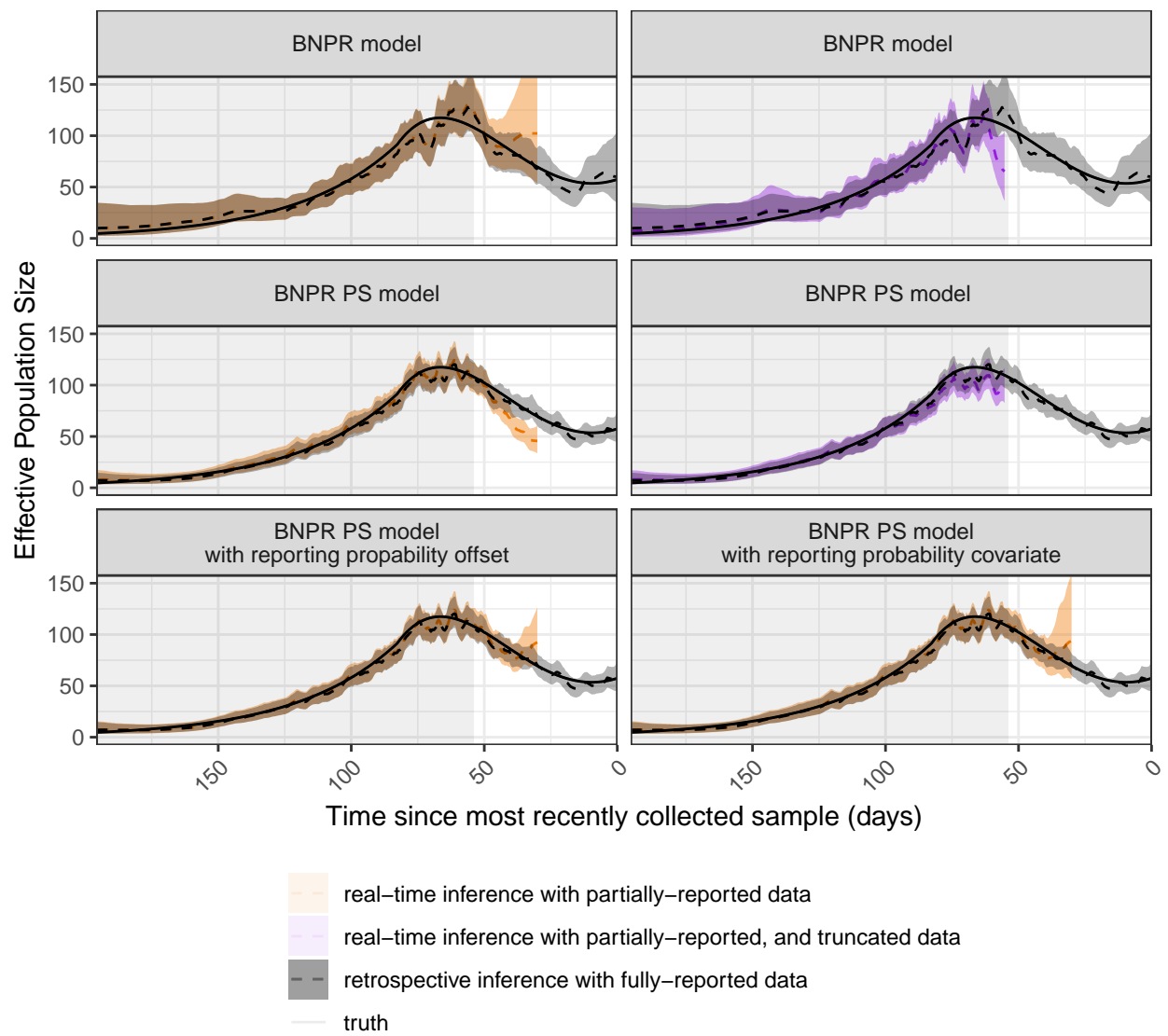


Figure S-9: Comparison of phylodynamic estimation methods of effective population size trajectory for three different simulated data scenarios from the scenario B trajectory.

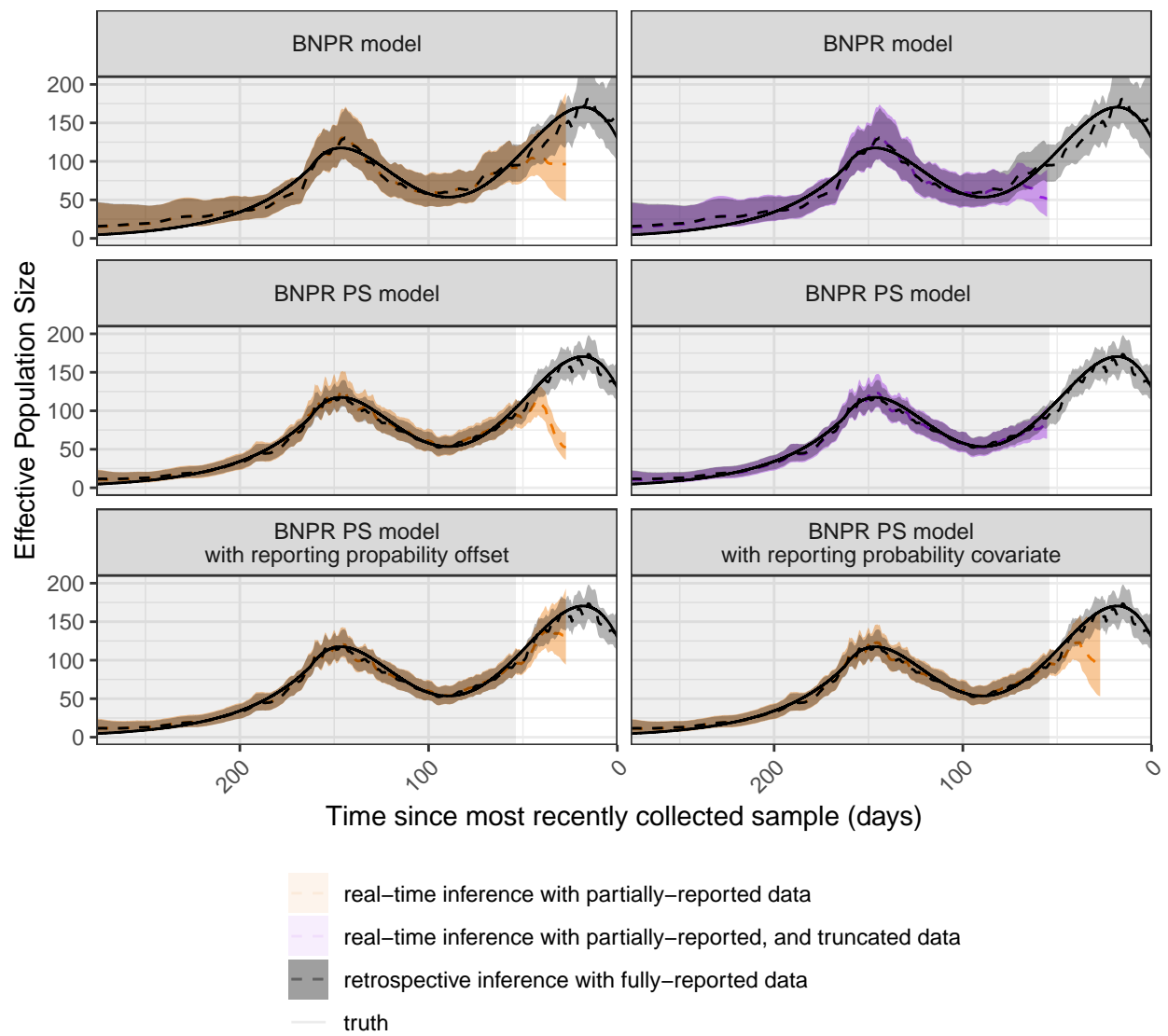


Figure S-10: Comparison of phylodynamic estimation methods of effective population size trajectory for three different simulated data scenarios from the scenario C trajectory.

## S-1.2.2 Performance metrics across all simulations

Table S-4: Mean relative deviation of effective population size from all estimation techniques in each data scenario for 500 simulations in scenarios A, B, and C. Time periods span from first simulated sampling time to 90th percentile of historic reporting delays, 55 days. The final time period for each simulation scenario spans from the first to last sampling time simulated.

Time period (days)	Retrospective		Real-time inference					
	BNPR	BNPR PS	Trunc. BNPR	Tunc. BNPR PS	BNPR	BNPR PS	BNPR PS with RP offset	BNPR PS with RP covariate
<b>Scenario A</b>								
[0,7)	-0.01	0.00			-0.36	-0.96	0.07	-0.50
[7,14)	0.01	0.00			-0.46	-0.95	0.00	-0.53
[14,21)	0.00	0.00			-0.38	-0.90	-0.02	-0.50
[21,28)	0.00	0.00			-0.23	-0.68	-0.04	-0.35
[28,35)	0.00	-0.01			-0.14	-0.51	-0.02	-0.24
[35,42)	0.00	-0.01			-0.03	-0.16	0.00	-0.06
[42,49)	0.01	-0.01			0.01	0.04	0.01	0.02
[49,56)	0.01	-0.01	-0.35	-0.12	0.01	0.06	-0.01	0.02
[0,156]	0.12	0.05	0.11	0.02	0.10	-0.01	0.04	0.01
<b>Scenario B</b>								
[21,28)	0.01	0.00			0.39	-0.54	0.20	0.18
[28,35)	0.00	0.00			0.22	-0.48	0.06	0.07
[35,42)	0.00	0.00			0.08	-0.27	-0.01	0.00
[42,49)	0.00	0.00			0.01	-0.08	0.00	0.00
[49,56)	0.00	0.00	-0.36	-0.07	0.00	-0.03	0.00	0.00
[0,229]	0.15	0.06	0.13	0.08	0.17	0.06	0.07	0.07
<b>Scenario C</b>								
[14,21)	-0.01	0.01			-0.06	-0.84	0.18	-0.26
[21,28)	0.00	0.01			-0.18	-0.67	-0.03	-0.27
[28,35)	0.00	0.00			-0.16	-0.55	-0.04	-0.23
[35,42)	0.00	0.00			-0.08	-0.28	-0.01	-0.10
[42,49)	0.00	0.00			-0.03	-0.08	0.00	-0.02
[49,56)	0.00	0.00	-0.46	-0.11	0.00	-0.02	0.00	-0.01
[0,307]	0.14	0.07	0.12	0.05	0.13	0.04	0.07	0.05



Table S-5: Percent of 95 percent Bayesian credible intervals that covered the true effective population size, from all estimation techniques in each data scenario for 500 simulations in scenarios A, B, and C. Time periods span from first simulated sampling time to 90th percentile of historic reporting delays, 55 days. The final time period for each simulation scenario spans from the first to last sampling time simulated.

Time period (days)	Retrospective		Real-time inference					
	BNPR	BNPR PS	Trunc. BNPR	Tunc. BNPR PS	BNPR	BNPR PS	BNPR PS with RP offset	BNPR PS with RP covariate
<b>Scenario A</b>								
[0,7)	99.13	97.97			100.00	0.00	100.00	100.00
[7,14)	99.20	98.48			100.00	0.00	100.00	100.00
[14,21)	99.25	98.75			100.00	0.00	100.00	90.91
[21,28)	99.19	98.74			99.20	0.00	99.70	90.16
[28,35)	99.45	99.12			97.80	3.30	98.05	88.91
[35,42)	99.54	98.88			98.56	74.88	98.26	95.61
[42,49)	99.46	98.55			99.57	98.32	98.11	98.51
[49,56)	99.13	98.56	81.81	93.91	99.23	98.15	98.47	98.69
[0,156]	98.36	96.71	97.42	96.68	98.83	89.72	97.57	97.10
<b>Scenario B</b>								
[21,28)	99.70	99.62			100.00	0.00	96.04	100.00
[28,35)	99.45	99.35			99.95	0.00	99.02	99.98
[35,42)	99.27	98.84			98.89	14.36	98.89	98.90
[42,49)	99.09	99.02			99.11	85.62	98.99	98.64
[49,56)	99.25	99.14	44.05	92.03	99.23	97.53	99.04	99.11
[0,229]	97.83	96.38	96.09	94.74	98.05	88.56	96.44	96.49
<b>Scenario C</b>								
[14,21)	98.72	98.54			100.00	0.00	100.00	100.00
[21,28)	99.80	99.21			99.53	0.00	99.37	95.91
[28,35)	99.31	98.59			98.27	0.00	98.33	89.99
[35,42)	99.50	98.87			97.12	20.17	98.43	91.60
[42,49)	99.68	99.50			99.19	90.77	98.82	98.35
[49,56)	99.19	98.97	32.32	92.99	99.42	98.84	99.08	99.16
[0,307]	97.86	96.15	95.46	96.48	98.32	91.67	96.77	96.61

Table S-6: Mean width of 95 percent Bayesian credible interval of effective population size from all estimation techniques in each data scenario for 500 simulations in scenarios A, B, and C. Time periods span from first simulated sampling time to 90th percentile of historic reporting delays, 55 days. The final time period for each simulation scenario spans from the first to last sampling time simulated.

Time period (days)	Retrospective		Real-time inference					
	BNPR	BNPR PS	Trunc. BNPR	Tunc. BNPR PS	BNPR	BNPR PS	BNPR PS with RP offset	BNPR PS with RP covariate
<b>Scenario A</b>								
[0,7)	38.90	23.77			530.38	9.86	583.96	208.03
[7,14)	29.59	19.36			262.33	8.94	306.41	120.18
[14,21)	27.00	17.13			164.57	10.44	155.74	77.54
[21,28)	24.62	15.46			99.80	16.86	63.91	54.50
[28,35)	22.49	14.08			66.95	17.33	39.84	41.11
[35,42)	20.59	12.94			34.46	20.61	24.48	24.51
[42,49)	18.84	11.93			24.46	20.31	17.88	18.87
[49,56)	17.22	10.96	30.12	24.04	21.32	17.39	14.60	15.76
[0,156]	17.60	10.71	15.91	9.87	20.76	12.11	13.27	13.47
<b>Scenario B</b>								
[21,28)	34.80	20.79			153.01	23.21	60.86	91.86
[28,35)	36.89	22.20			116.57	22.09	43.01	74.10
[35,42)	39.54	23.89			72.47	24.03	30.70	43.77
[42,49)	41.89	25.81			50.06	27.78	28.68	30.44
[49,56)	43.87	27.80	65.45	36.93	47.67	30.36	29.88	30.25
[0,229]	30.73	18.44	30.96	18.00	35.40	20.32	20.10	21.98
<b>Scenario C</b>								
[14,21)	68.83	46.38			375.50	28.30	273.68	200.07
[21,28)	67.69	45.33			225.11	38.12	128.97	147.24
[28,35)	64.90	42.95			169.17	36.12	88.34	114.28
[35,42)	61.57	39.90			101.09	41.18	58.65	66.72
[42,49)	57.18	36.53			68.31	43.16	45.50	45.75
[49,56)	53.04	33.49	63.02	48.23	59.05	39.49	38.77	39.00
[0,307]	47.22	28.35	44.08	27.42	50.66	30.03	30.76	32.15

Boxplot of posterior median of preferential sampling coefficient, by estimation strategy and simulation scenario

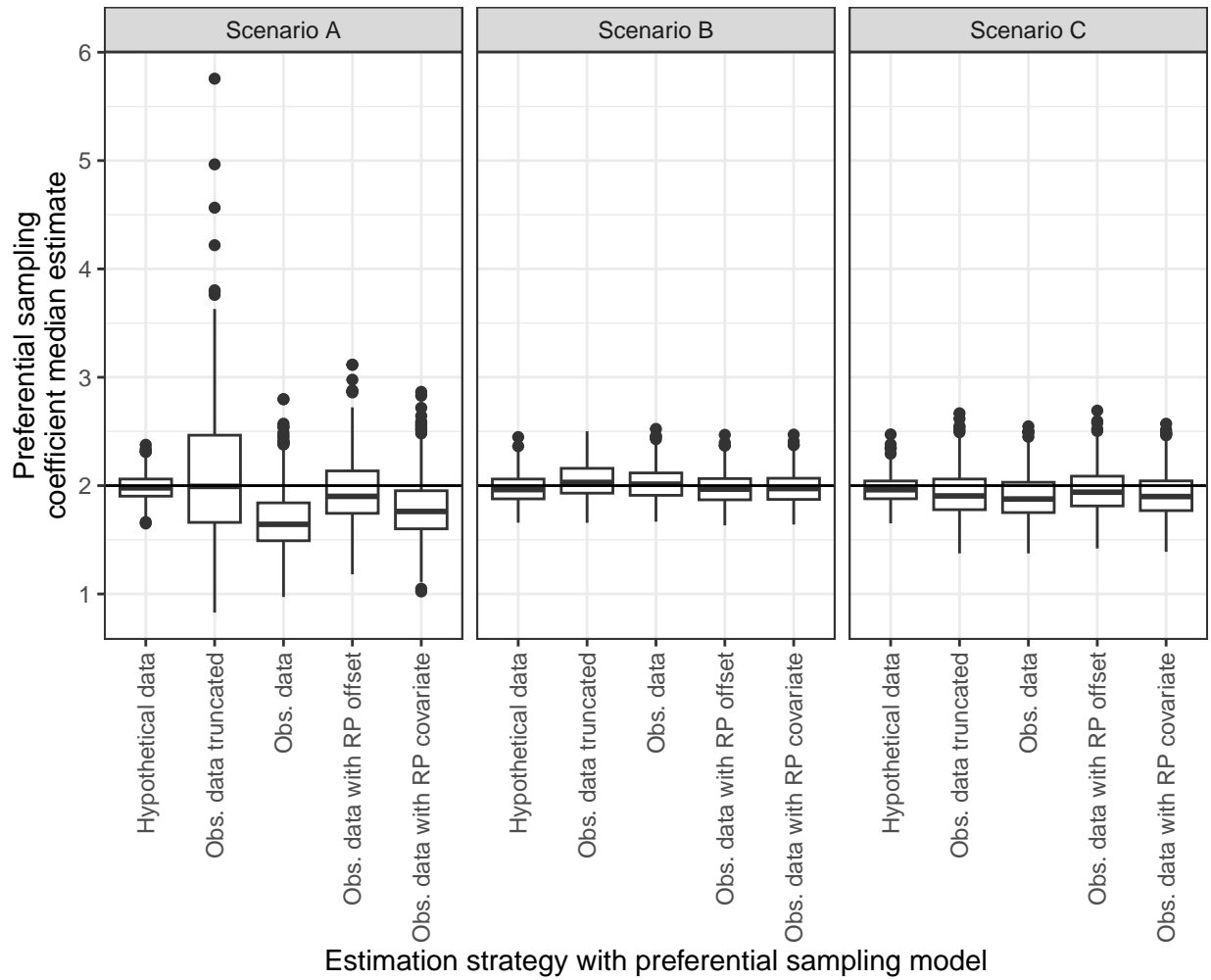


Figure S-11: Median preferential sampling coefficient estimate from simulations by estimation strategy and simulation scenario.

## S-2 Real data investigation: Washinton state COVID dynamics

### S-2.1 Sequences from GISAID

#### Data Availability

GISAID Identifier: EPI\_SET.240619zd

doi: 10.55876/gis8.240619zd

All genome sequences and associated metadata in this dataset are published in GISAID's Epi-CoV database. To view the contributors of each individual sequence with details such as accession number, Virus name, Collection date, Originating Lab and Submitting Lab and the list of Authors, visit [10.55876/gis8.240619zd](https://gisaid.org/gis8.240619zd)

#### Data Snapshot

- EPI\_SET.240619zd is composed of 500 individual genome sequences.
- The collection dates range from 2021-02-01 to 2021-08-01;
- Data were collected in 1 countries and territories;
- All sequences in this dataset are compared relative to hCoV-19/Wuhan/WIV04/2019 (WIV04), the official reference sequence employed by GISAID (EPI\_ISL\_402124). Learn more at <https://gisaid.org/WIV04>.

Table S-7: BEAST modeling details for each real data scenario for Washington State samples reported to GISAID. All unnoted specifications were left as BEAST defaults.

	Full Scenario	Observed Scenario	Truncated Scenario
Data	Sampled before 2021-08-01, inclusive	Reported before 2021-08-01, inclusive	Sampled before 2021-06-21, inclusive
Models			
Substitution	HKY	HKY	HKY
Clock type	strict	strict	strict
Coalescent	Bayesian Skygrid	Bayesian Skygrid	Bayesian Skygrid
# of parameters	50	50	50
Last transition	1.63 years	1.52 years	1.6 years
Priors			
Kappa	LogNormal(1, 1.25)	LogNormal(1, 1.25)	LogNormal(1, 1.25)
Frequencies	Dirichlet(1, 1)	Dirichlet(1, 1)	Dirichlet(1, 1)
Clock rate	Unif(3e-4, 1.1e-3)	Unif(3e-4, 1.1e-3)	Unif(3e-4, 1.1e-3)
Root height	None (tree prior only)	None (tree prior only)	None (tree prior only)
Skygrid precision	Gamma(0.001, 1000)	Gamma(0.001, 1000)	Gamma(0.001, 1000)
MCMC options			
Chain length	2e+07	2e+07	2e+07
Burn in	2500000	2500000	2500000
Log every	2000	2000	2000
Seed	-	-	-

## S-2.2 BEAST modeling details for real data investigation: Washington State

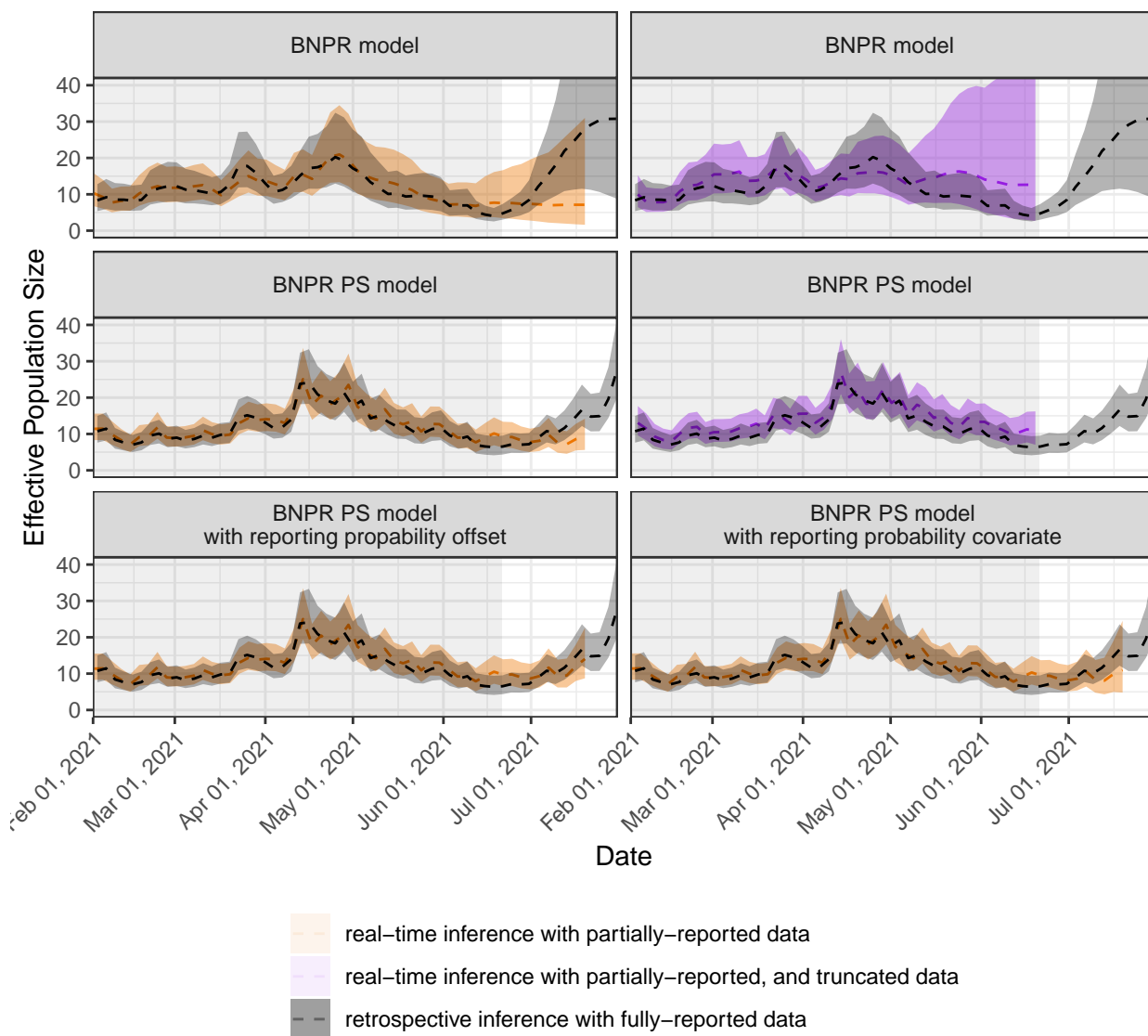


Figure S-12: Comparison of phylodynamic estimation methods of effective population size trajectory for Washington State SARS-CoV-2 sequences.